DAP/ LANGLEY NAG1-568

CR.

82668

ASL ✓

P.106

MIT AERONAUTICAL SYSTEMS LABORATORY REPORT

ASL 87-1

AN EXPERIMENTAL LOW REYNOLDS NUMBER COMPARISON OF A WORTMANN FX67-K170 AIRFOIL, A NACA 0012 AIRFOIL, AND A NACA 64-210 AIRFOIL IN SIMULATED HEAVY RAIN

Anthony P. Craig
and
R. John Hansman

FINAL REPORT TO THE NASA LANGLEY RESEARCH CENTER
ON WORK ACCOMPLISHED UNDER RESEARCH GRANT NAG-1-568

June 1987

AN EXPERIMENTAL LOW REYNOLDS NUMBER COMPARISON OF A WORTMANN FX67-K170 AIRFOIL, A NACA 0012 AIRFOIL, AND A NACA 64-210 AIRFOIL IN SIMULATED HEAVY RAIN

ABSTRACT

Wind tunnel experiments were conducted on Wortmann FX67-K170, NACA 0012, and NACA 64-210 airfoils at rain rates of 1000 mm/hr and Reynolds numbers of 310,000 to compare the aerodynamic performance degradation of the airfoils and to attempt to identify the various mechanisms which affect performance in heavy rain conditions. Lift and drag were measured in dry and wet conditions, a variety of flow visualization techniques were employed, and a computational code which predicted airfoil boundary layer behavior was used. At low angles of attack, the lift degradation in wet conditions varied significantly between the airfoils. The Wortmann section had the greatest overall lift degradation (~25%) and the NACA 64-210 airfoil had the smallest (~5%). At high angles of attack, the NACA 64-210 and NACA 0012 airfoils had improved aerodynamic performance in rain conditions due to an apparent reduction of the boundary layer separation. Performance degradation in heavy rain for all three airfoils at low angles of attack could be emulated by forced boundary layer transition near the leading edge. Time resolved measurements indicate two primary mechanisms are responsible for the observed performance degradation. The initial effect of rain is to cause premature boundary layer transition at the leading edge. The secondary effect occurs at time scales consistent with top surface water runback times (1-10 seconds). The runback layer is thought to effectively alter the airfoil geometry. This effect is, most likely, exaggerated due to the small scale of the tests. When the airfoils were waxed, the performance in wet conditions was further degraded compared with unwaxed, wet conditions. The severity of the performance degradation for the airfoils varied. The relative differences appeared to be related to the susceptibility of each airfoil to premature boundary layer transition.

TABLE OF CONTENTS

PAGE __3__ INTENTIONALLY BLANK

PRECEDING PAGE BLANK NOT FILMED

LIST OF FIGURES

NOMENCLATURE

A   wind tunnel cross sectional area

A_f airfoil frontal cross sectional area

α angle of attack

β local collection efficiency

β_t total collection efficiency

c   airfoil chord length

c_p pressure coefficient

c_L lift coefficient

c_D drag coefficient

c_M moment coefficient

$c_{d,d}$ drag coefficient due to droplet momentum transfer

D   rain droplet diameters

D_d drag force due to droplet momentum transfer

F_L lift force

F_D drag force

F_S surface forces

* FT   a forced transition point

ϕ contact angle

h   droplet height

h_o projected height of the airfoil

L/D   lift to drag ratio

LWC   liquid water content

λ empirical constant

$\dot{m}$ mass flow rate of impacting water

n_O empirical constant

NR   nozzle flow rate, vol/time

$n(D)$ droplet distribution function

ν kinematic viscosity

π empirical constant

* R   a reattachment point

Re   Reynolds number

RR   Rain rate, mm/hr

ρ local air density

ρ_a freestream air density

ρ_w water density

S   airfoil surface area

* S   a separation point

s   airfoil surface length

T   water runback time

* T   a transition point

t   airfoil thickness

t_w water layer thickness

V   local velocity

V_∞ freestream velocity

v   local water runback velocity

y_O local droplet impact height

y_{ol} lower tangent droplet trajectory limit

y_{ou} upper tangent droplet trajectory limit

* used in figures to mark boundary layer behavior

11

Chapter 1

INTRODUCTION

1.1 Heavy Rain

Typical heavy rainfall rates observed world wide are on the order of 150-250 mm/hr with durations of approximately one minute[17]. However, higher rainfall rates can be expected for shorter periods. The world record rate is 1828.8 mm/hr [24], although sustained rain rates greater than 500 mm/hr are rarely observed. Often, heavy rain occurs during thunderstorms and is associated with microbursts where strong wind shear conditions may also be present.

Heavy rain may alter the aerodynamic flight characteristics of an aircraft. For example, significant performance degradation has been observed on high performance laminar flow sailplanes when operating in rain conditions. The high glide ratio of the aircraft decreases significantly when encountering rain conditions.

Aircraft normally have brief encounters with heavy rain. However, these brief encounters can be dangerous because they often occur at low altitudes and are accompanied by other hazardous weather phenomenon such as wind shear. Several aircraft accidents have been partially attributed to heavy rain[15].

The potential performance penalty incurred by aircraft operating in heavy rain may become critical in wind shear

encounters. The rain may alter the flight characteristics by effectively increasing the stall speed and lowering the stall angle of attack. Current wind shear escape procedures suggest that if necessary, the pilot fly below 'bug speed', the normally accepted minimum flight speed, in order to gain the increased climb capability[20]. During this procedure, the aircraft is operating near 'stick shaker' speed, the aircraft's stall speed in dry conditions with a small safety margin included. In this flight regime, smooth control of pitch attitude is necessary to avoid 'stick shaker' overshoots and to ensure appropriate maneuver and stall margins. Heavy rain may alter the aerodynamic characteristics of the wing, reducing or eliminating the margin between the 'stick shaker' and the actual stall angle. In this case, directing the crew to fly at 'stick shaker' speed may induce stall.

1.2 Potential Effects of Heavy Rain on Aircraft

Rain may affect aircraft performance in a number of ways:

1) Increases Airfoil Roughness. The water presence on the airfoil increases the roughness of the airfoil. This effect can cause premature transition of the boundary layer from laminar to turbulent flow, which can, in turn, drastically change the aerodynamic characteristics of the airfoil. The most likely airfoil performance changes due to

13

premature boundary layer transition would be to increase the drag, decrease the lift, and alter stall behavior.

2) Alters Airfoil Geometry. A water film on the airfoil may act to thicken the airfoil and effectively alter the airfoil geometry. However, film thicknesses are normally less than 2 mm. A typical 10% thick airfoil with a 3 meter chord will change thickness by less than 1% in rain conditions. Generally, very slight changes in airfoil shape will not significantly alter aerodynamic performance.

3) Imparts Momentum. The impacting raindrops impart momentum to the aircraft in both the horizontal and vertical directions. For a Boeing 747 in a 2000 mm/hr rainstorm, horizontal momentum transfer due to rain has been calculated to result in a horizontal drag force equivalent to a deceleration of 0.75 knots/s or 9% of the maximum thrust provided by the engines[15]. In a 100 mm/hr rainstorm the equivalent force corresponds to a deceleration of 0.04 knots/s [15]. Considering the typical time spent in a heavy rain encounter, the total drag force created by the momentum transfer is minimal. While the momentum of the impacting drops may have a small effect on aircraft performance, it is unlikely to be a major consideration in flight through rain. Vertical forces generated by momentum transfer are even less significant. Downward pressures of less than 0.04 pounds/ft^2 have been estimated[23]. This is only a 0.03% increase for a typical transport aircraft wing

14

loading of 150 pounds/ft^2.

4) <u>Increases Total Weight</u>. The water film on the aircraft increases the aircraft's total weight. However, rain weight has been estimated to be less than 1% of the total weight for typical commercial aircraft[23] and can be neglected.

1.3 <u>Previous Experimental Observations</u>

A number of previous wind tunnel experiments have been conducted on airfoils in simulated heavy rain conditions. In low Reynolds number wind tunnel experiments (Re=3.1*10^5), Hansman and Barsotti[16] report maximum L/D losses of up to 75% for a natural laminar flow airfoil in heavy rain conditions.

The heavy rain program at the NASA Langley Research Center tested several airfoils in heavy rain conditions at a Reynolds number of 1.7*10^6. In these tests, Dunham et al[11] observed reductions of up to 20% in the maximum lift coefficient for a transport type airfoil in landing configuration (multi-element airfoil with a single slat and 2 component flap) under simulated heavy rain (figure 1.1a). The loss of lift was accompanied by an increase in drag and a reduction of up to 8° in the stall angle of attack. However, for the same airfoil in cruise configuration as shown in figure 1.1b, minimal performance degradation in heavy rain conditions at low angles of attack and unexpected increases in aerodynamic performance at high angles of attack were

15

measured. Dunham[10] also reports a 15% decrease in the
maximum lift coefficient for both a flapped and unflapped
NACA 0012 airfoil in heavy rain conditions as shown in figure
1.2.

a) 64-210 flapped model   b) 64-210 unflapped model
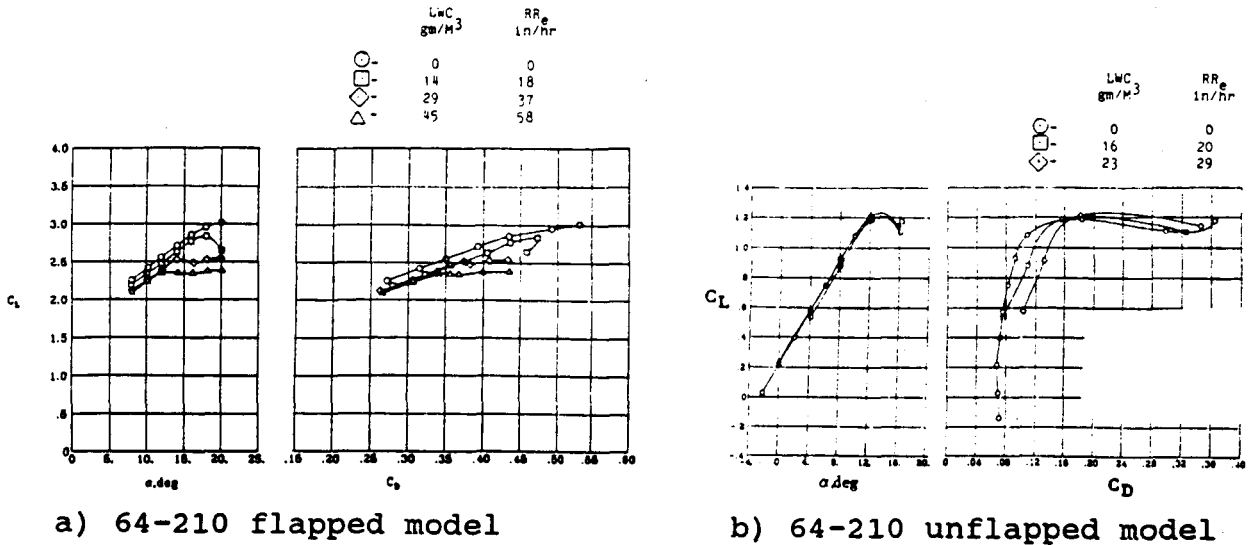
Figure 1.1. Lift and drag measurements in dry and wet
   conditions on a NACA 64-210 airfoil model in landing
   configuration, single slatted and double flapped (a) and on
   a NACA 64-210 airfoil model in cruise configuration,
   unflapped (b). (ref. 10)

a) 0012 flapped model   b) 0012 unflapped model
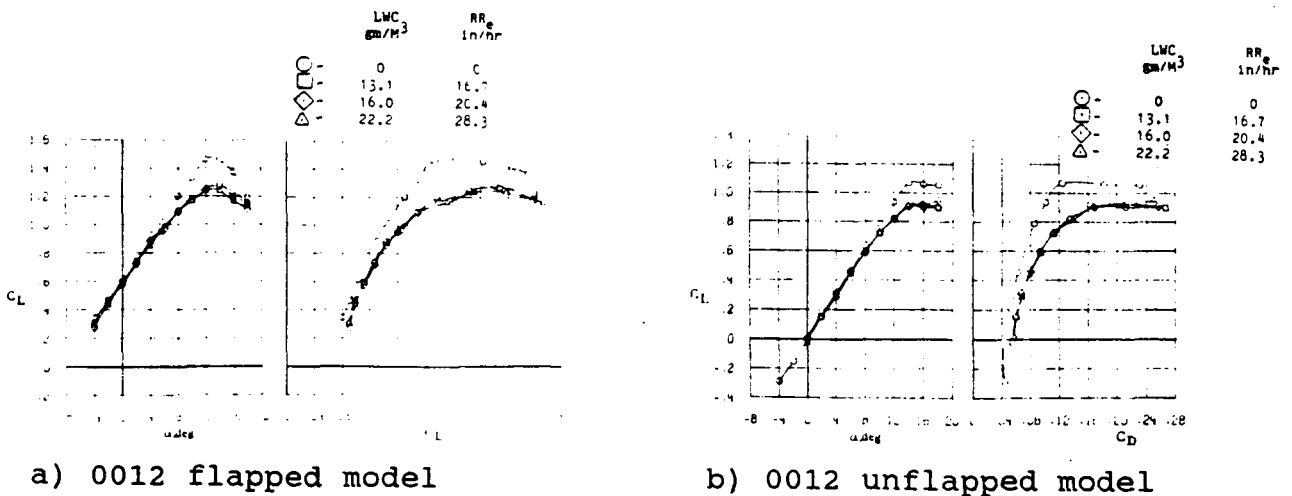
Figure 1.2. Lift and drag measurements in dry and wet
   conditions on a NACA 0012 airfoil model with a single flap
   deployed (a) and on a NACA 0012 unflapped airfoil model
   (b). (ref. 10)

16

1.4 Thesis Approach and Overview

Because of the significant variations in aerodynamic performance degradation observed for different airfoils in heavy rain conditions, a comparative study was conducted on three different airfoils in dry and rain conditions. Wind tunnel experiments were conducted on Wortmann FX67-K170, NACA 0012, and NACA 64-210 airfoils to determine the magnitude and causes of performance degradation in heavy rain.

These airfoils were chosen because they are typical of the various designs which are currently used for different aircraft applications. The Wortmann airfoil is a thick, laminar flow airfoil which is representative of the high lift to drag airfoils used on sailplanes. The NACA 64-210 airfoil is a thin, naturally turbulent airfoil, typically found on transport category aircraft. The NACA 0012 falls between the other two airfoils, and has been a baseline airfoil for much aerodynamic testing in the past. In addition, all three airfoils have been previously tested in rain conditions.

The maximum chord Reynolds number in the tests was limited to $3.1*10^5$ due to wind tunnel considerations. Various experiments were conducted to determine the mechanisms which alter the airfoils' aerodynamic performance in heavy rain conditions. Both steady-state, dry and wet conditions, as well as time-dependent, transient effects were investigated. Lift and drag measurements were recorded for

various test conditions. Flow visualization techniques were developed to observe water runback behavior and aerodynamic boundary layer behavior. In addition, a compressible, viscid airfoil computational fluid dynamics code was employed to gain additional insight into the airfoils' boundary layer aerodynamics.

This thesis presents the results of these experiments. Chapter 2 discusses scaling considerations for experimentally investigating aerodynamic performance in heavy rain conditions. Low Reynolds number boundary layer behavior and typical water runback phenomena are also presented. Chapter 3 describes the experimental techniques used to investigate the performance degradation of the airfoils in rain conditions. The experimental configuration for the wind tunnel tests, the flow visualization and data acquisition techniques, and the computational methods are described in this chapter. Chapter 4 presents the results of the wind tunnel experiments for each of the three airfoils, and chapter 5 summarizes the findings.

Chapter 2

EXPERIMENTAL SCALING ANALYSIS

2.1 Overview

The subscale experimental testing of airfoils in rain conditions presents a difficult scaling problem. Three different scaling areas must be considered. The first area which must be considered is the scaling of the aerodynamic performance of the airfoil. The second scaling consideration is related to the freestream rain condition, and the associated droplet impact with the airfoil. The third scaling area is related to the water layer buildup and runback behavior on the airfoil. The exact scaling laws for investigating rain effects in small scale wind tunnel tests have not been determined, although at least one scheme has been suggested[3]. It is difficult to match all the parameters of the problem consistently. In fact, it may be impossible to define a closed system which consistently resolves all the heavy rain scaling issues at subscales. In the following sections, an analysis of some of the experimental scaling issues will be made.

2.2 Aerodynamic Considerations

Airfoil lift and drag forces are normally non-dimensionalized to lift and drag coefficients with a standard force parameter ($\frac{1}{2}\rho_a V_\infty^2 S$) where ρ_a is the air density, V_∞ is

19

the freestream velocity, and S is the area of the wing surface, i.e.

$$c_L = F_L \ / \ (\tfrac{1}{2} \rho_a V_\infty^2 S) \qquad\qquad (2\text{-}1)$$

$$c_D = F_D \ / \ (\tfrac{1}{2} \rho_a V_\infty^2 S) \qquad\qquad (2\text{-}2)$$

Normally baseline airfoil performance is determined by assuming an inviscid flow condition. In this case, lift and drag performance of an airfoil as a function of angle of attack is independent of the non-dimensionalizing force parameter, $(\tfrac{1}{2} \rho_a V_\infty^2 S)$.

When viscous effects are considered in airfoil aerodynamics, the Reynolds number becomes an important parameter. The chord Reynolds number is the ratio of inertial forces to viscous forces acting on the airfoil, i.e.

$$Re = V_\infty \ c \ / \ \nu \qquad\qquad (2\text{-}3)$$

where V_∞ is the freestream velocity, c is the airfoil chord length, and ν is the fluid kinematic viscosity. At high chord Reynolds numbers above approximately 10^6, viscosity effects and the influence of the boundary layer are minor. In this regime, the non-dimensional lift and drag performance of an airfoil as a function of angle of attack is nearly equivalent to the inviscid 'baseline' case. As the Reynolds number is decreased to about 10^5 however, viscosity and

boundary layer effects become more important, and the non-dimensionalized lift and drag performance of an airfoil begins to vary with the force parameter. In this regime, Reynolds number effects must be considered.

The Reynolds number gives an indication of the boundary layer behavior and its importance to the overall aerodynamic performance of the airfoil. When testing at lower Reynolds numbers, high Reynolds number performance is normally simulated by fixing the boundary layer transition point. The airfoil then becomes effectively independent of Reynolds number.

Because of wind tunnel limitations, the Reynolds number used for the tests described in this thesis was only 310,000. Some ambiguity may exist in determining the rain effects on the airfoils due to Reynolds number considerations. Therefore, direct application of the results obtained in the experimental tests to larger scale cases may not be appropriate. However, the mechanisms which affect airfoil performance in rain conditions are likely similar at larger scales.

2.2.1 Typical Low Reynolds Number Airfoil Boundary Layer Behavior[19]

At Reynolds numbers greater than approximately 10^6, airfoil boundary layer behavior is fairly stable and can be well predicted. Laminar to turbulent boundary layer

21

transition occurs within a small, well predicted region on the airfoil. Small changes in Reynolds number, angle of attack, or other flight parameters will not drastically alter the transition location or the overall boundary layer behavior.

However, at a chord Reynolds numbers between $1*10^5$ and $5*10^5$, the airfoil boundary layer behavior is highly dependent on the airfoil geometry (airfoil surface pressure distribution) and angle of attack. The boundary layer behavior becomes complicated in this regime with mechanisms present which induce transition and cause separation.

A typical airfoil upper surface boundary layer at low Reynolds numbers is depicted in figure 2.1.
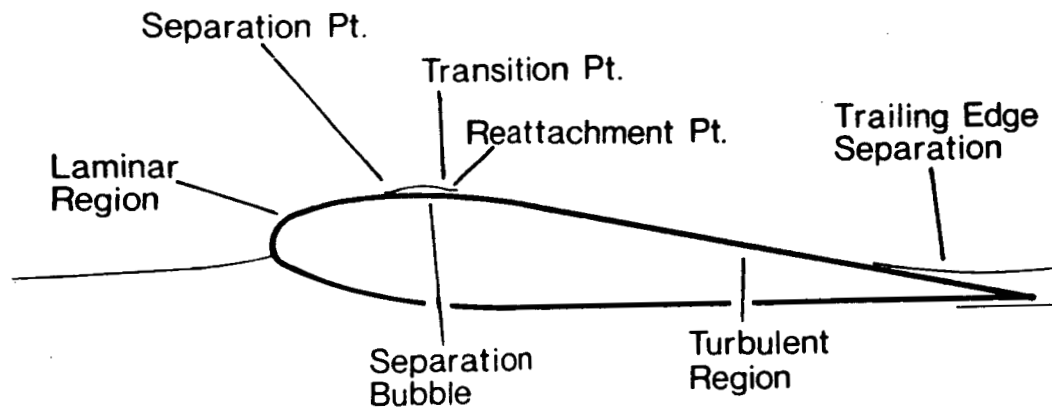
Figure 2.1. Typical upper surface boundary layer behavior for a low Reynolds number airfoil.

The laminar boundary layer in this figure separates from the airfoil, undergoes transition, becomes turbulent and

reattaches to the airfoil, forming a laminar separation bubble. The laminar separation bubble is able to reattach because the turbulent boundary layer has additional energy which is associated with the turbulent mixing. The reattached turbulent boundary layer grows rapidly as it progresses downstream where it becomes increasingly susceptible to separation. Therefore, trailing edge separation is often present at low Reynolds numbers as exemplified in figure 2.1. Contrary to high Reynolds number flows, small changes in airfoil geometry, angle of attack, or Reynolds number may significantly alter the boundary layer behavior for low Reynolds number airfoils. These effects are described below.

a) Effect of Airfoil Geometry. The location and length of a laminar separation bubble on an airfoil is highly dependent on the airfoil geometry (airfoil surface pressure distribution). Two examples of 'typical' top surface laminar separation bubbles and their respective pressure distributions are shown in figure 2.2. In figure 2.2a, the boundary layer behavior of a 'typical' thin airfoil is shown. It has a small leading edge radius which induces a high suction peak followed by a strong adverse pressure gradient. An adverse pressure gradient is defined as a region on the airfoil where the surface static pressure is increasing downstream. The pressure distribution on the thin airfoil results in a small laminar separation bubble just aft of the
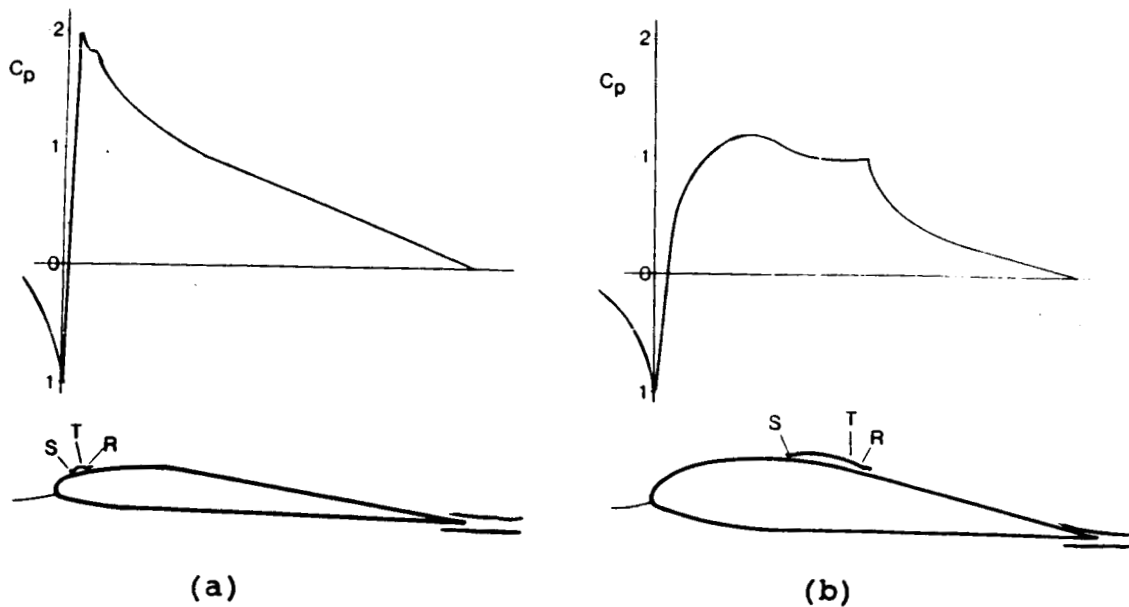
S   Separation Pt.
T   Transition Pt.
R   Reattachment Pt.

Figure 2.2. Effect of airfoil geometry on pressure
   distribution and low Reynolds number boundary layer
   behavior. Thin airfoil is shown on left (a), thick airfoil
   is shown on right (b).

suction peak.   In figure 2.2b, a 'typical' thick airfoil is

shown.   The pressure distribution on the thick airfoil is

smoother than for the thin airfoil.   This results in a longer

separation bubble on the thick airfoil that is located

farther aft when compared to the thin airfoil.

24

b) <u>Effect of Angle of Attack</u>.   The length of the separation bubble generally decreases as the airfoil's angle of attack is increased, and it moves forward with the increasing adverse pressure gradient present at higher angles of attack.   This boundary layer behavior is depicted in figure 2.3.   If the angle of attack is further increased, the separation bubble may burst which results in a leading edge stall as shown in figure 2.3c.   This is a very sudden, abrupt, and dramatic stall which occurs when the separated boundary layer is suddenly unable to reattach to the airfoil because of the excessively steep pressure gradient present at the increased angle of attack.

c) <u>Effect of Reynolds Number</u>. As the Reynolds number of an airfoil is decreased, the viscous forces become more important, and the boundary layer transition point moves aft. If a laminar separation bubble is present, the bubble length will correspondingly increase with the decreasing Reynolds number as shown in figure 2.4.   In some cases, the boundary layer may transition aft of the airfoil trailing edge which would result in an unattached laminar separation bubble as shown in figure 2.4c.

2.3 <u>Scaling of Simulated Rain for Experimental Tests</u>

The second scaling area to consider for subscale testing is related to the freestream rain condition.   Simulating natural rain conditions when conducting small scale tests is

S   Separation Pt.
T   Transition Pt.
R   Reattachment Pt.

(a)

Increasing
Angle of
Attack

(b)

(c)
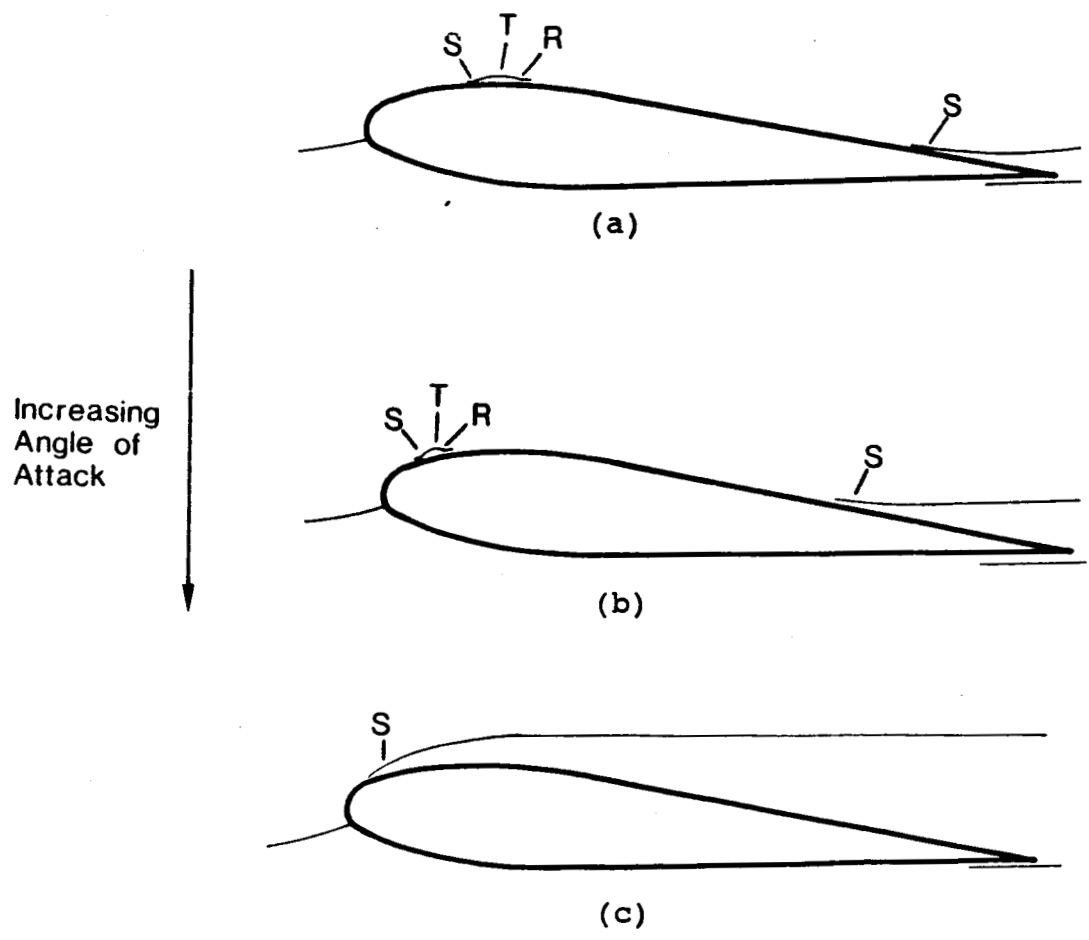
Figure 2.3.   Effect of angle of attack on low Reynolds number
  boundary layer behavior.
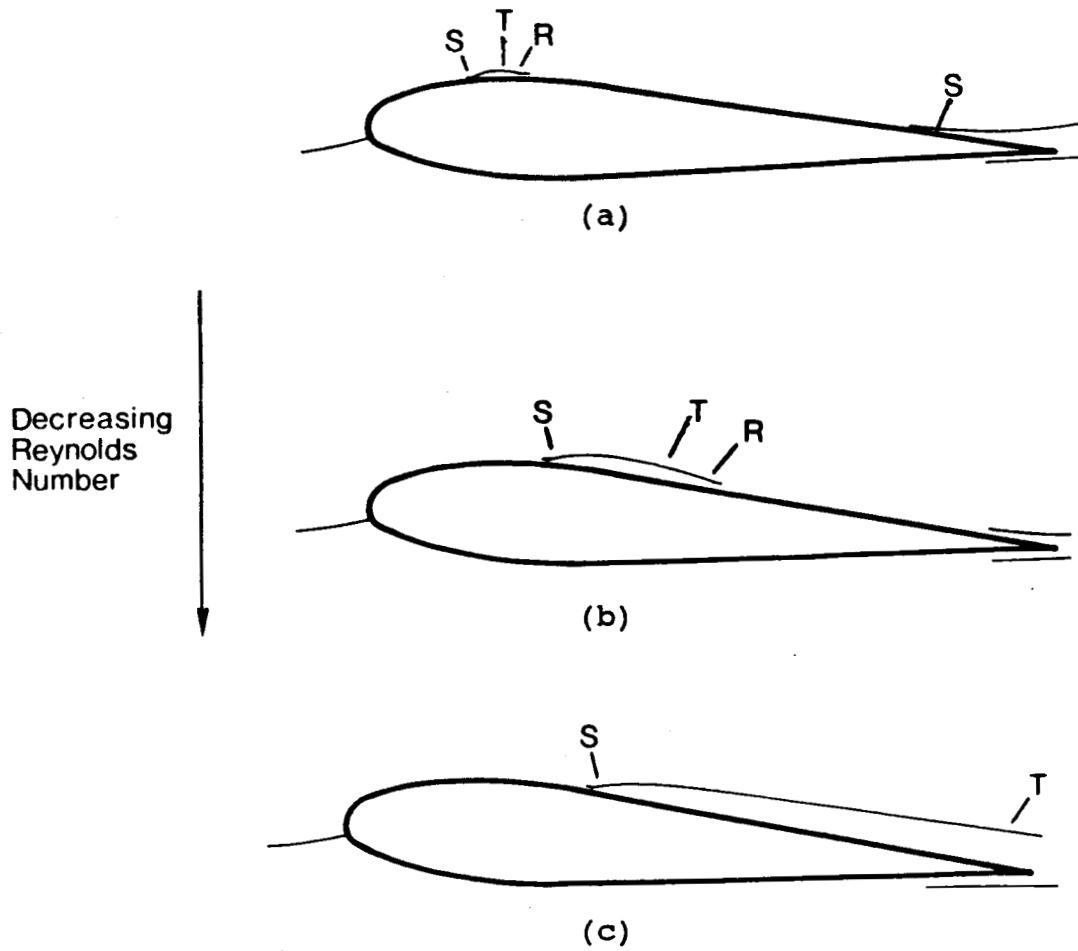
Figure 2.4.   Effect of Reynolds number on low Reynolds number boundary layer behavior.

complicated. Laws for matching the experimental rain
conditions to natural conditions are not well defined. There
are a number of points which must be addressed when
introducing rain at these small scales.

2.3.1 Determination of Rain Rate and Liquid Water Content

One important parameter to match in experimental tests
is natural rain rate. One method to match these quantities
is to match the liquid water contents.

a) Natural Conditions. The natural rain liquid water
content can be calculated knowing the spectrum of droplet
diameters associated with a given rain rate by,

$$LWC = (\pi/6 * 10^{-3}) \, \rho_w \int_0^\infty D^3 \, n(D) \, dD \qquad (2-4)$$

where ρ_w is the density of water in gm/cm^3, D is the droplet
diameter, and $n(D)$ is the droplet distribution[21]. A
Marshall-Palmer distribution is one approximation which is
often used to express the number of rain droplets of a given
size at a known rain rate. The distribution is given by,

$$n(D) = n_o e^{-\lambda D} \qquad (2-5)$$

where n_o and λ are empirical constants determined by
observation of natural rainfall and are $8*10^3$ and

$4.1*(RR)^{-0.21}$ respectively where RR is the assumed rain rate in mm/hr. Equation 2-4 can be numerically integrated for a given rain rate over the raindrop spectrum to yield the equivalent liquid water content. For the experimental tests, a rain rate of 1000 mm/hr was chosen. Numerically integrating equation 2-4 results in an equivalent liquid water content of 29.45 g/m^3.

b) Experimental Conditions. To determine the experimental liquid water content, the water nozzle flow rate, wind tunnel velocity, and wind tunnel size must be known. Assuming the water droplets travel at the freestream tunnel velocity and that they are distributed evenly over the entire cross section of the wind tunnel, the experimental liquid water content can be calculated as,

$$LWC = (NR * \rho_w) / (V_\infty * A) \qquad (2-6)$$

where LWC is the liquid water content, NR is the nozzle flow rate in volume/time, ρ_w is the water density, V_∞ is the freestream velocity, and A is the wind tunnel cross sectional area.

2.3.2 Water Collection Rates on the Airfoil

One important parameter which is related to the total water collection rate is the local collection efficiency, β.

29

It defines the amount of water impacting a specific area of the airfoil and is based on the freestream droplet trajectories. The local collection efficiency is defined as the ratio between the freestream droplect trajectory separations, dy_o, and the corresponding impact length on the airfoil body, ds, i.e.

$$\beta = dy_o / ds \qquad\qquad (2\text{-}7)$$

as shown in figure 2.5. The local collection efficiency at a given location on the airfoil is determined by a number of different factors.
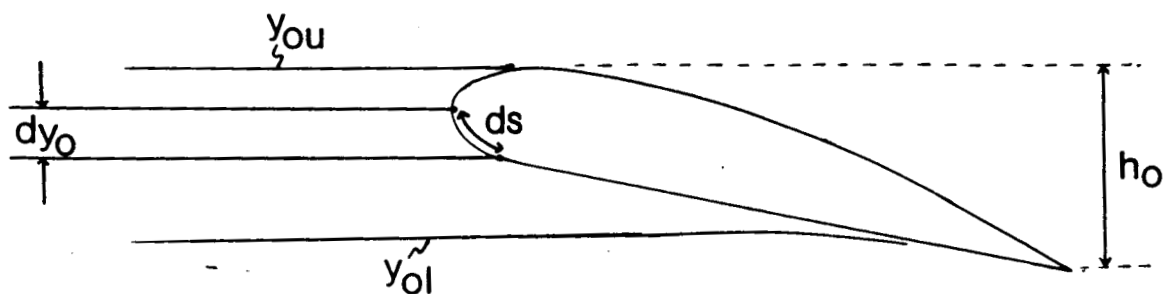
Figure 2.5. Illustation of impingement terminology and water droplet trajectories.

One important factor which determines the local collection efficiency is the airfoil angle of attack. An example of the effect of angle of attack is shown in figure 2.6. The angle of attack determines the area of the droplet impact zone which is the region on the airfoil where the local collection efficiency is not zero (figure 2.6). At higher angles of attack, more water may be collected because the frontal impact area is effectively increased.
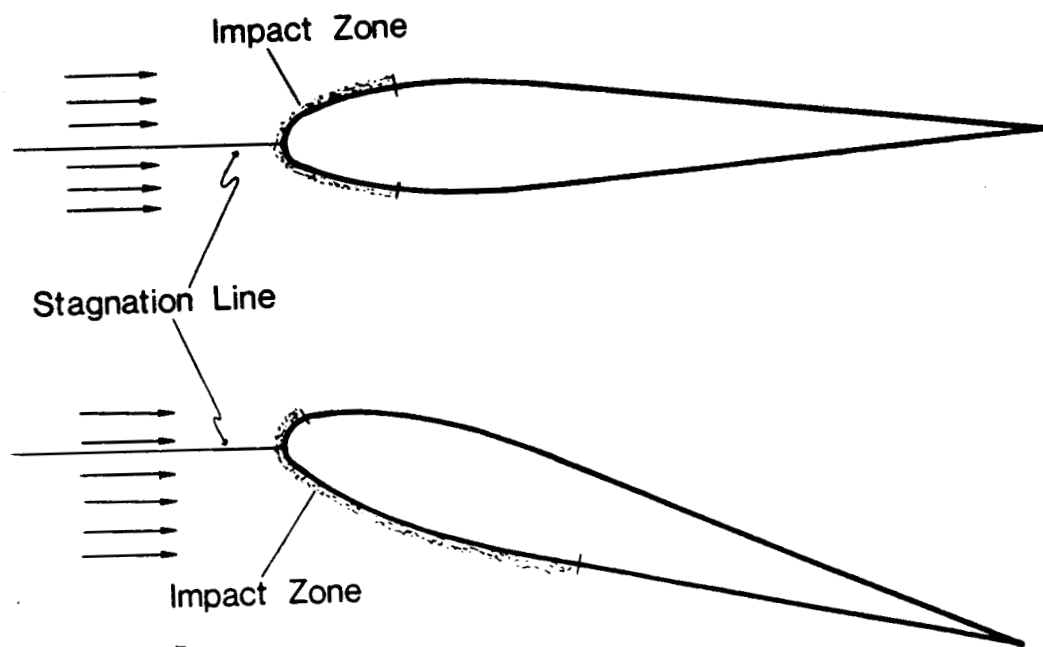
Figure 2.6. Effect of angle of attack on local collection efficiency.

The second factor which determines the local collection efficiency is droplet motion around the airfoil due to aerodynamic forces. This effect is governed by the droplet sizes and airfoil pressure distribution. Smaller droplets are more easily influenced by the flow around the airfoil and result in a lower local collection efficiency. For typical precipitation droplet sizes of order 1 mm, however, the effects of aerodynamic forces on droplet motion are minimal, and the droplet trajectories are nearly straight lines.

To find the total airfoil collection efficiency, β_t, the local collection efficiency can be integrated over the entire airfoil, i.e.

$$\beta_t = (y_{ou} - y_{ol}) / h_o \qquad\qquad (2\text{-}8)$$

where y_{ou} and y_{ol} are the upper and lower tangent trajectory limits shown in figure 2.5, and h_o is the projected height of the body along the vertical coordinate line.

The total collection efficiency, β_t, is then used to find the mass flow rate of water impacting an airfoil, $\dot{m}$, by

$$\dot{m} = (\overline{LWC})(V_\infty)(A_f)(\beta_t) \qquad\qquad (2\text{-}9)$$

where LWC is the freestream liquid water content, V_∞ is the freestream velocity, and A_f is the airfoil frontal cross sectional area. The airfoil frontal cross sectional area,

32

A_f, is constant, not dependent on angle of attack, and when analyzing two-dimensional cases, is the airfoil thickness, t.

One additional effect of the local collection efficiency deals with differences in total top and bottom surface collection amounts. Depending on the location of the leading edge stagnation line with respect to the impact droplets, different top and bottom total water collection rates will be induced[5],[13]. This effect can be seen figure 2.6. At low angles of attack, the water droplets impact nearly equally on the top and bottom surfaces. However, at higher angles of attack, the lower airfoil surface collects a higher proportion of the impinging water droplets, and so very low water collection rates on the upper surface of an airfoil may result. This effect will become important when the water runback phenomenon is considered in section 2.4.

2.3.3 Momentum Transfer Due To Droplet Impact

For typical scale flight conditions, the momentum transfer due to droplet impact is considered insignificant (section 1.3). However, the drag induced by droplet impact momentum transfer must be appraised.

The induced drag force due to droplet impacts can be estimated by approximating their impact momentum transfer. The mass flow rate of water impacting the airfoil, $\dot{m}$, is given in equation 2-9. Assuming the drops travel at the freestream wind tunnel velocity before hitting the airfoil

and then rebound with equal and opposite velocity, the drag
induced by the droplet momentum transfer, D_d, is,

$$D_d = 2V_\infty \dot{m} \qquad\qquad (2\text{-}10)$$

The drag force can now be non-dimensionalized with respect to
the standard airfoil force parameter $(\frac{1}{2}\rho_a V_\infty^2 S)$,

$$c_{d,d} = D_d / (\frac{1}{2}\rho_a V_\infty^2 S) \qquad\qquad (2\text{-}11)$$

to yield the induced drag coefficient on the airfoil due to
droplet momentum transfer. The drag calculated above due to
droplet impacts is an upper limit, and it gives a first
indication of the potential importance of this effect. One
interesting result of equation 2-11 is that it can be shown
that it is independent of airfoil size.

2.4 Water Runback Considerations and Scaling

The third scaling area which must be considered when
testing airfoils in rain conditions is associated with the
water layer presence and water runback phenomenon. The
physical development of the water layer and the related
scaling issues will be described below.

2.4.1 The Water Runback Layer

a) Local Collection Efficiency. The local collection

efficiency defines the droplet impact distribution and the total amount of water which will be present on the top and bottom surfaces of an airfoil. These effects are described in section 2.3.2.

b) <u>Water Runback Development</u>. When rain is first initiated, a transitional water runback period exists before the fully developed quasi-steady wet condition on the airfoil has evolved. Initially, water is only present where the water droplets impact the airfoil. In this area, the local collection efficiency is not zero.

As the total water volume increases in the impact zone, droplets and rivulets form which begin to move aft.

c) <u>Droplet Motion</u>. Droplet motion on surfaces has been studied previously in detail[14]. A droplet/surface interaction is shown in figure 2.7. Its motion is characterized by a balance of the aerodynamic forces and the surface adhesion forces, i.e.,

$$(\rho v^2 h) / F_s \qquad\qquad (2\text{-}12)$$

where ρv^2 characterizes the dynamic pressure force on the droplet, h is the droplet height, and F_s represents the total surface forces. In general, if this ratio (equation 2-12) is high, then the water droplet will move smoothly, and if it is low, then the droplets will be stationary.
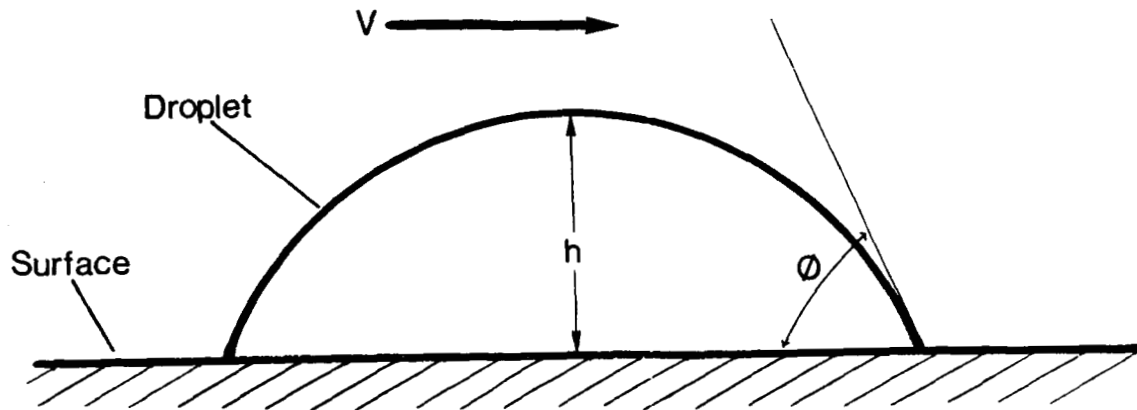
Figure 2.7.   Illustration of the droplet/surface interaction
    terminology.

One important additional parameter of the droplet is the
contact angle, ϕ , which is shown in figure 2.7.   Increasing
the contact angle effectively increases the droplet height
and may also alter the surface force characteristics.

When analyzing droplet dynamics, the actual droplet
motion quickly becomes very complex.   Receding and advancing
contact angles as well as other nonlinear effects are
normally observed[14].

d) Rivulet Motion.   Rivulet motion, depicted in figure
2.8, is similar to droplet motion where the droplet dynamical
pressure forces are transformed into rivulet pressure and
shear forces, shown in figure 2.8.   The pressure force is
generated by the water height and the internal water flow
rate.   The shear forces are induced by the local velocity
distribution above the rivulet.   Rivulet pressure and shear

36

forces are normally smaller than equivalent droplet dynamic forces, so rivulets typically move slower than droplets of the same height.

Increasing the rivulet contact angle increases the rivulet height which, in turn, increases the likelihood of rivulet breakup. In this case, the rivulet may deteriorate into droplets. In addition, there are nonlinear contact angle effects and hysteresis which are associated with the rivulet motion.
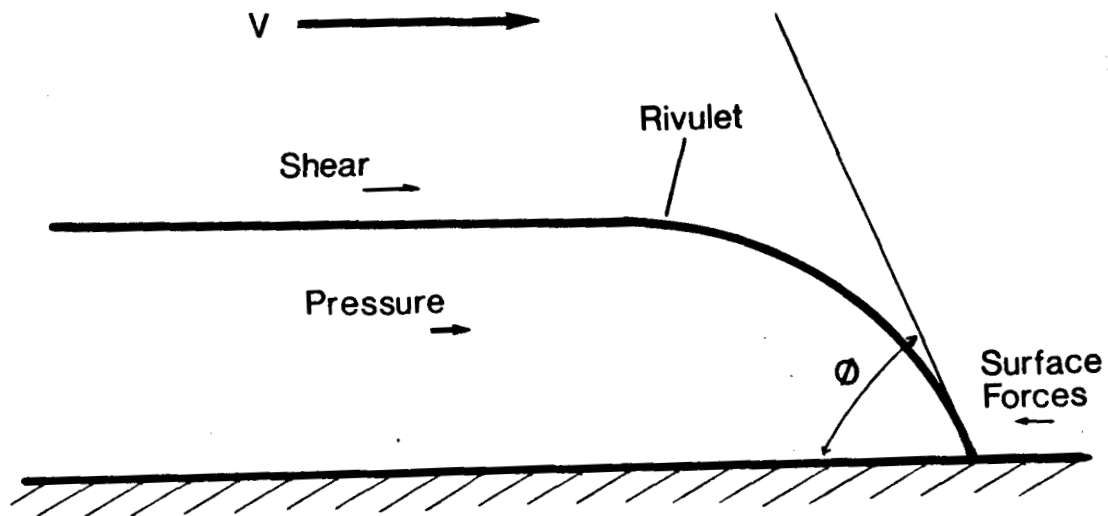
Figure 2.8. Illustration of rivulet terminology.

e) Effects of Water Feeding Rates on Rivulet Motion. As introduced above, the rivulet has one important additional feature which does not appear in droplet motion. Water is able to flow through the rivulet from the impact area. This

37

allows the rivulet size to increase or decrease depending on its forward motion and the water feeding rates. The water collection rate, $\dot{m}$, governs the rivulet growth potential and is a determining factor in the pressure forces.

When the water collection rate is low, the rivulet remains thin and the pressure forces are small. This results in reduced rivulet runback velocities and in some cases, the rivulet may stagnate. If the rivulet becomes stationary, it remains stationary and can increase in size. When the pressure forces have increased enough to overcome the surface forces, the rivulet will begin moving again. There is a hysteresis effect associated with this motion which is parallel to the hysteresis effect of static and dynamic friction.

When the water collection rates are low as they may be on the top surface of an airfoil at high angles of attack, the water rivulet can deteriorate into individual droplets. When this occurs, the droplets normally runback at increased velocities because the drag force on the droplets is higher compared to the rivulet condition.

2.4.2 Scaling Water Layer Thickness

The relative thickness of the water layer on an airfoil, t_w, is an important physical scaling parameter. In this analysis, a two-dimensional airfoil is considered, and it is assumed that the airfoil size will not influence the airfoil

38

pressure distribution, the total collection efficiency, β_t, or the water/surface runback behavior. As a first approximation, then, the water layer thickness distribution, t_w, is related only to the airfoil pressure distribution, c_p, and the amount of water on the airfoil per unit airfoil length, $\dot{m}/c$, i.e.

$$t_w(t,x) = t_w(\dot{m}(t)/c, c_p(x)) \qquad (2-13)$$

where the amount of water on the airfoil is governed by the water collection rate of the airfoil. The pressure distribution can be non-dimensionalized with respect to the airfoil chord, as

$$c_p(x) \longrightarrow c_p(x/c) \qquad (2-14)$$

The amount of water on the airfoil, given by $\dot{m}/c$, can also be shown to be independent of the airfoil chord, i.e.

$$\dot{m}(t) = (LWC)(V_\infty)(t)(\beta_t(\alpha)) \qquad \text{(from 2-9)}$$

$$\dot{m}(t) / c = (LWC)(V_\infty)(t)(B_t(\alpha)) / c$$

$$\qquad = (LWC)(V_\infty)(t/c)(B_t(\alpha))$$

$$\dot{m}/c \ (t) = \dot{m}(t/c) \qquad (2-15)$$

Therefore, the water layer thickness, given in equation 2-13, is independent of airfoil chord, i.e.

$$t_w(t,x) \longrightarrow t_w(t/c, x/c) \qquad\qquad (2\text{-}16)$$

Equation 2-16 shows that for a given airfoil, angle of attack, freestream liquid water content, and freestream velocity, the water layer thickness over the airfoil will be independent of the airfoil size. In other words, the water layer thickness distribution will remain constant with increasing or decreasing airfoil size.

Typical maximum water layer thicknesses have been observed to be on the order of one millimeter for subscale tests at freestream velocities of approximately 31.3 m/sec. In this case, for a 6 inch (15.24 cm) chord airfoil which is 10% thick, the ratio of water layer thickness to airfoil thickness is about 1:15. Hence, the water layer thickness may alter the airfoil shape by 10% or more at a typical location on the airfoil. For a full scale airfoil of chord 3 meters, this thickness ratio drops to about 1:300, so an airfoil thickness change of less than 1% would be expected. Therefore, water layer effects may be important in small scale tests, but they are probably negligible in full scale applications.

2.4.3 Scaling Water Runback Time

The transient time between dry and fully developed wet conditions may be an important parameter when considering the

performance effects of an aircraft which encounters rain conditions. The performance changes will not stabilize until the water layer has reached a quasi-steady distribution. One time constant, directly related to the total time needed to reach fully developed wet conditions, is the runback time scale.

In general, the runback time is defined as the time a droplet or rivulet requires to runback from the airfoil's leading edge to the trailing edge. If the local runback velocity, $v(x)$, is known as a function of the distance, x, from the airfoil leading edge, then the runback time may be obtained by integrating this velocity over the airfoil chord, c, as,

$$T = \int_0^c \frac{dx}{v(x)} \qquad (2-17)$$

If boundary layer behavior and surface tension effects at varying scales are neglected, then the runback velocity, $v(x)$, is a function of the amount of water on the airfoil and the driving forces acting on that water due to the pressure distribution, and both of these can be non-dimensionalized with respect to airfoil chord (equations 2-16, 2-14). Then the runback velocity distribution can also be non-dimensionalized with chord length, and equation 2-17 can be transformed to

$$T = c \int_0^1 \frac{d(x/c)}{v(x/c)} \qquad (2\text{-}18)$$

The integral part of this equation is constant for a given airfoil and rain condition independent of airfoil size. This shows that the rivulet runback time should scale directly with chord length as would be expected.

The time needed for the overall water layer distribution to reach quasi-steady conditions is directly related to the rivulet runback time, so as a first approximation, the total transient dry to wet time will scale with chord length.

Chapter 3

INVESTIGATION TECHNIQUES

3.1 Overview

Experimental methods were employed to study the performance degradation of airfoils in heavy rain conditions. A wind tunnel was used to study various aspects of the airfoils' aerodynamic behavior. Because of the complex physical phenomena involving both time and spacial variables, unique analysis techniques were developed. The water layer presence caused difficulties in visualization of aerodynamic flow behavior. However, various methods were simultaneously developed to visualize both aerodynamic and surface water behavior.

In addition to the experimental analysis, a computational airfoil code[8,12] was used to gain additional insight. The code predicted two-dimensional airfoil aerodynamic performance including boundary layer behavior.

3.2 Wind Tunnel Set-Up

Figure 3.1 is a schematic view of the wind tunnel set up used for the experiments. The airfoils had a 6 inch chord (15.24 cm) and a 1 foot span (30.48 cm) and were held in the 1 ft by 1 ft MIT low turbulence wind tunnel by a 2-component external force balance. For experimental purposes, the airfoil's angle of attack was referenced to the airfoil's
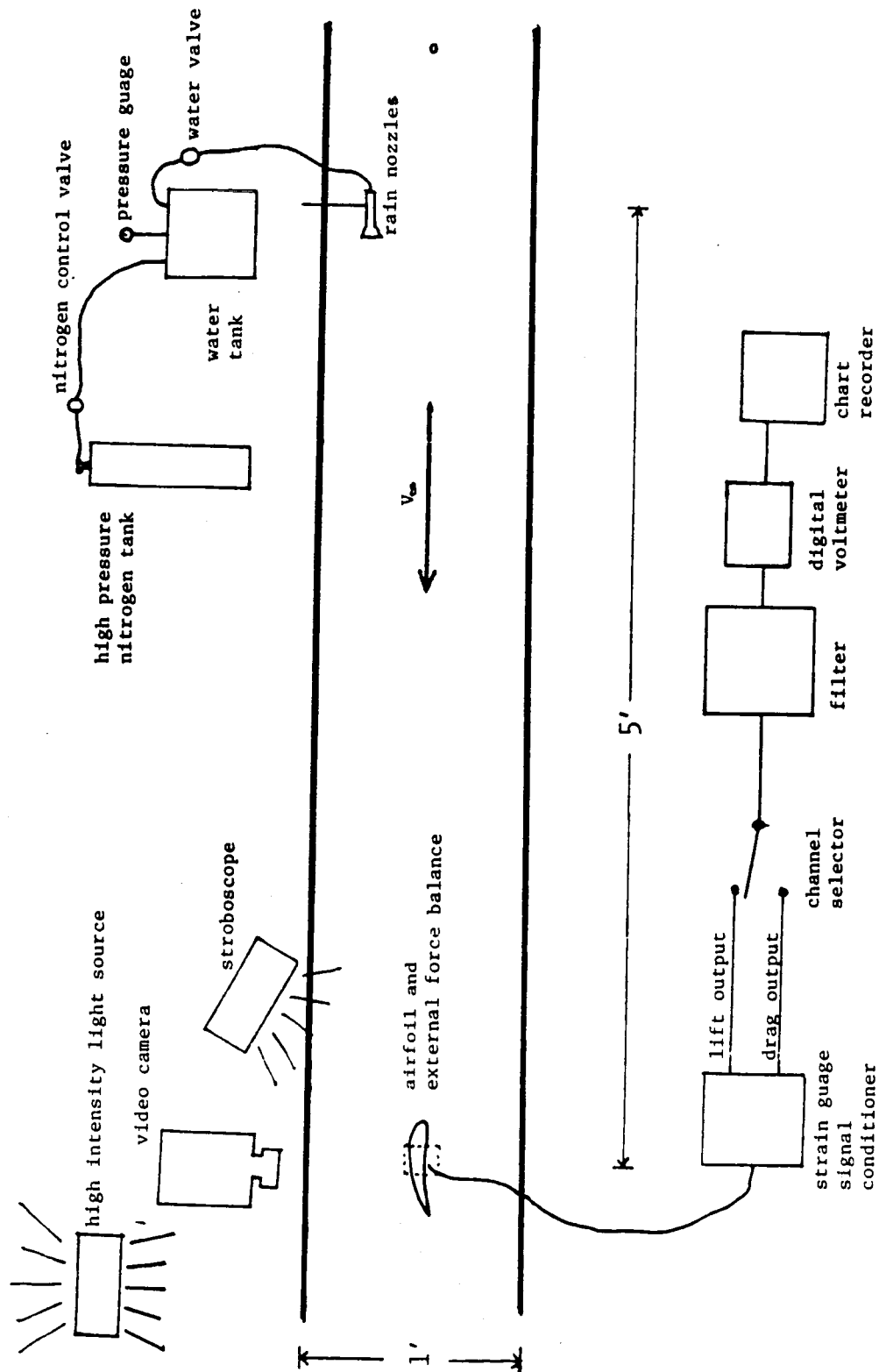
Figure 3.1. Schematic view of the wind tunnel set-up.

mean geometric chord line. Typical angle of attack measurement precision was $\pm$ 0.5°.

The freestream tunnel velocity was measured upstream of the nozzles by a conventional pitot tube, micro-manometer system. A freestream velocity of 31.3 m/s (70 mi/hr) was normally used for the wind tunnel tests corresponding to a chord Reynolds number of 310,000.

Water droplets were introduced 1.5 meters (5 ft) upstream of the airfoil by three rain simulation nozzles placed on the top and sides of the wind tunnel. The nozzles pointed downstream and were positioned to generate an even distribution of droplets in the test area. The droplet diameters produced by these nozzles varied principly within the range of 0.3 to 0.9 mm.

The liquid water content (LWC) in the wind tunnel, could be controlled by varying the internal pressure of the water tank supplying the nozzles. A high pressure nitrogen tank and control valve regulated pressure in the water tank. Liquid water content was calculated in the wind tunnel by experimentally calibrating water tank pressure with nozzle flow rates. From equation 2-6, with a nozzle flow rate of 5300 ml/min and freestream velocity of 31.3 m/s (70 mi/hr), a liquid water content of 30 g/m^3 was used as a test case. This corresponds to a rain rate of approximately 1000 mm/hr.

45

3.3 Airfoils Tested

The three airfoils chosen for the comparison are shown in figure 3.2. They include a:

1) Wortmann FX67-K170

2) NACA 0012

3) NACA 64-210

(coordinates are given in the appendix). These sections were chosen because each is designed to operate with slightly different aerodynamic characteristics. The Wortmann airfoil is a low drag, naturally laminar flow airfoil typically used on sailplanes. It is designed to have a laminar boundary layer over at least 50% of the chord which it uses to enhance it aerodynamic efficiency. In high performance sailplanes, the Wortmann section has been found to be operationally susceptible to heavy rain.

The NACA 64-210 airfoil is designed to operate with a turbulent boundary layer and is similar to those used on transport category aircraft in cruise configuration. The NACA 0012 airfoil was chosen because it is a simple, symmetric airfoil and was expected to have intermediate boundary layer behavior.

In addition, all three airfoils were tested previously in heavy rain conditions. The Wortmann airfoil was tested by Hansman and Barsotti[16], and the NACA 64-210 and 0012 airfoils were part of a joint effort with the NASA Langley Research Center to investigate scaling behavior of rain effects.
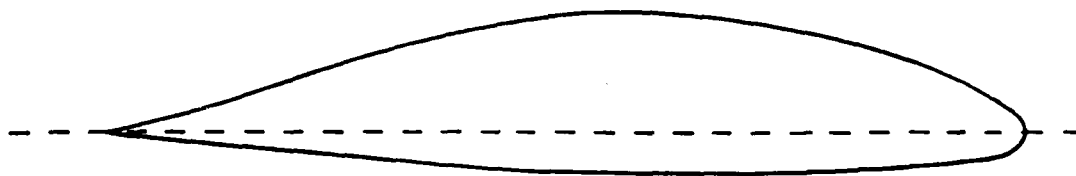
WORTMANN FX67-K170
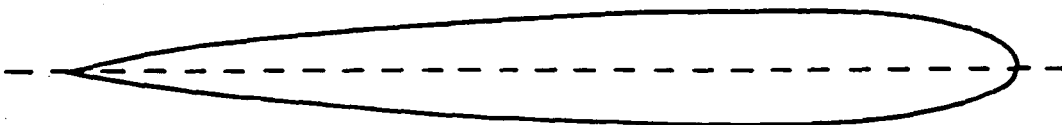
NACA   0012
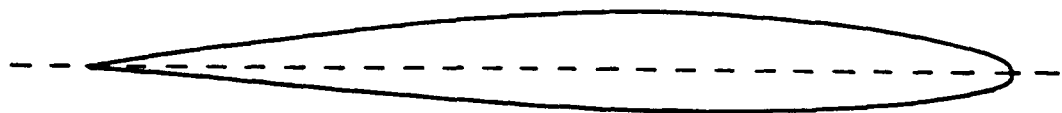
NACA   64-210

Figure 3.2. Airfoil sections tested in rain conditions.

3.3.1 Waxing to Vary Airfoil Surface Chemistry

In order to vary surface chemistry properties on the airfoils, wax was applied. The contact angle of the airfoil/water interface was changed from approximately 50° for the unwaxed airfoil to nearly 90° for the waxed airfoil. Contact angle is defined as the angle a drop of liquid makes at a surface, and its significance is described in section 2.4.1. A number of coats of wax were applied to the airfoils initially. The airfoils were rewaxed as necessary to maintain the test condition.

3.3.2 Forcing Boundary Layer Transition by Trip Strips

In an attempt to model the aerodynamic roughening effect of rain, boundary layer transition elements were placed on the airfoils. These elements cause the boundary layer to transition prematurely from laminar to turbulent flow by increasing the boundary layer instability. The transition point is a function of the level of disturbances in the flow. By placing roughness elements on the airfoil, the transition point can be moved and controlled.

Sand grains were used as boundary layer forcing elements. The sand grains used for these tests measured approximately 0.635 mm to 1.015 mm diameter which is larger than the minimum sand grain size normally suggested by Rae and Pope[22]. These grains efficiently transitioned the boundary layer where they were placed without showing any

48

other adverse aerodynamic behavior.

Figure 3.3 shows an airfoil with a strip of roughness elements in place. Two different techniques were used to apply the sand grains to the airfoils. In the first, clear paint was used as the binding agent. The second method used double sided thin clear tape as the adhering agent. Both methods yielded good results.
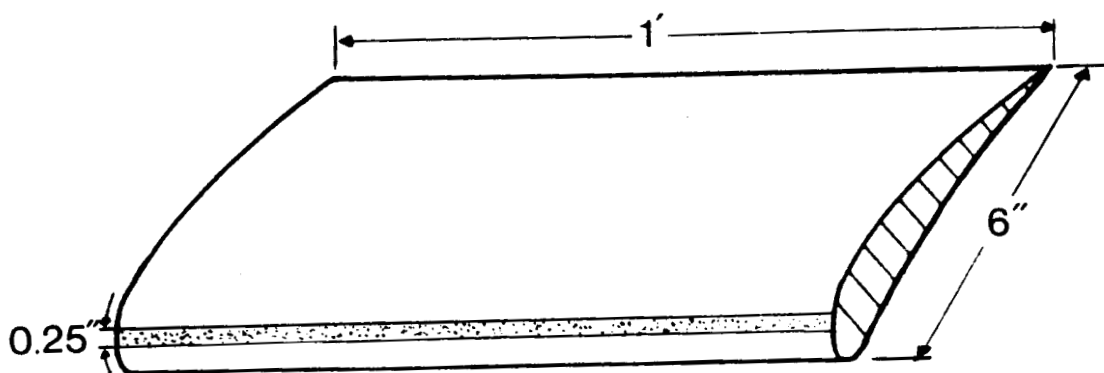
Figure 3.3. Illustration of an airfoil with a trip strip in place.

3.4 Lift and Drag Measurements

Force measurements were made on the airfoils by a 2-axis external strain gauge force balance that measured lift and drag. Voltage outputs from the strain gauges on the force balance were first passed through a strain gauge signal conditioner and then through a low pass filter (figure 3.1). The resulting voltage outputs could then be recorded and with predetermined calibration data, converted directly to force

49

measurements. The force balance was calibrated regularly using known weights. The calibration curves were linear across the entire range of forces measured on the airfoil, and the voltage/force conversion constants did not change over time. Due to the comparative nature of these tests, no corrections were made to the data due to wind tunnel blockage effects.

3.4.1 Steady-State Force Measurements

When steady-state lift and drag measurements were made, the voltage outputs were low pass filtered at 0.5 hz in order to attenuate the high frequency noise in the signals which is caused by an aeroelastic force balance effect. This was done to obtain steady voltage outputs which could then be easily recorded from the digital voltmeter. The filter and other electronics were always included when strain gauge force calibrations were made.

3.4.2 Time-Dependent Force Measurements

In order to record time-dependent force data, a chart recorder was employed. A filter was again necessary in this test condition because the force balance had a natural oscillation frequency of approximately 11 hz which was excited by the aerodynamic behavior. This rather strong 11 hz signal had to be removed before reasonable detail could be seen in other aspects of the time-dependent data. The
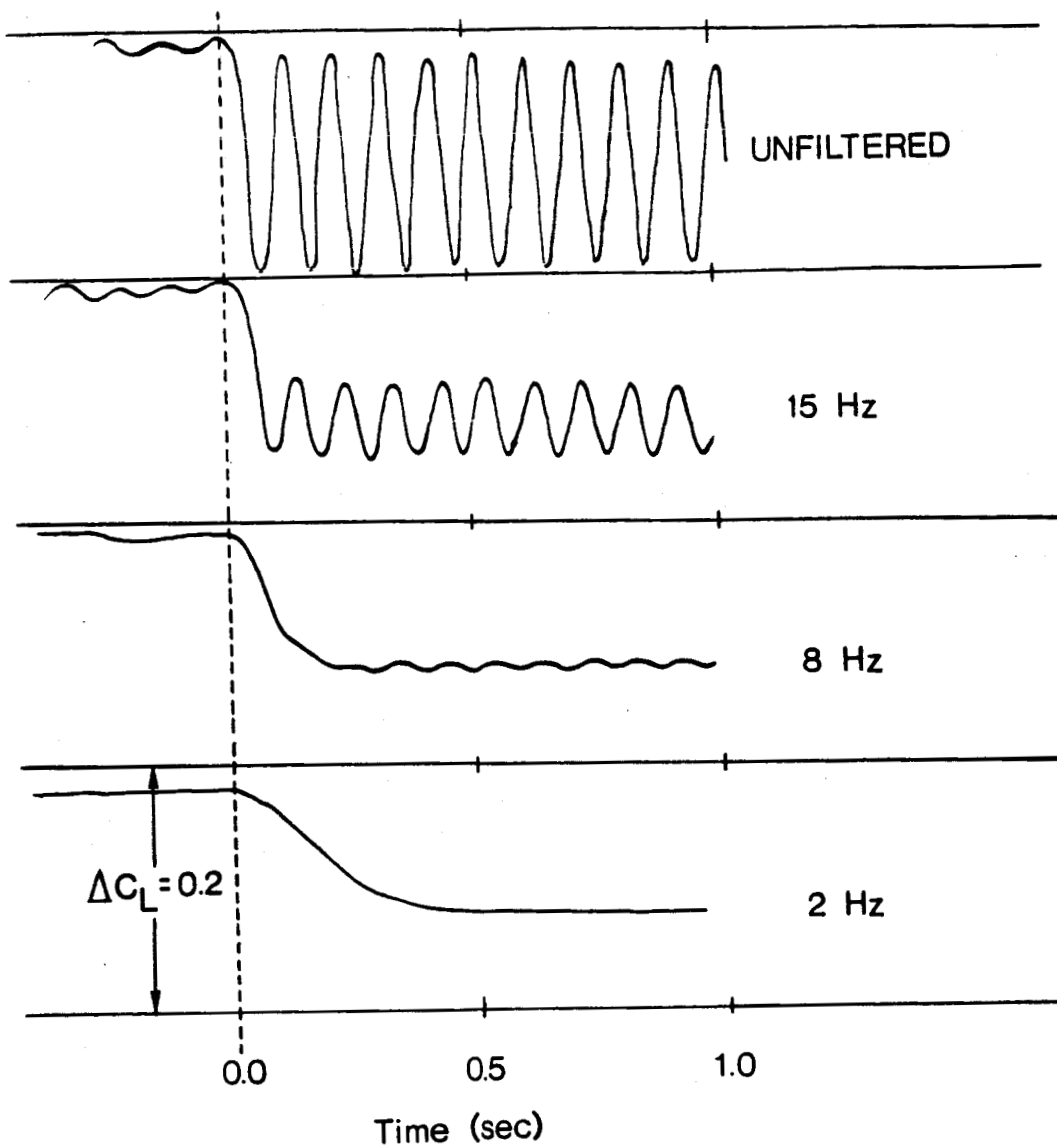
Figure 3.4. Step response of the force balance with respect
   to low pass filter frequency.

passband of the low pass (analog) filter was set as high as

possible in this case, typically 10 hz, in order to retain a

fast output response time and still filter the undesired

11 hz signal.   Figure 3.4 shows the step response of the

balance as a function of the low pass filter frequency, and

indicates the time constants associated with an instantaneous input. To generate the step input, a string was attached to the force balance, given a constant force load, and then cut with scissors. The magnitude of the step input in figure 3.4 is indicated by an equivalent lift coefficient change. In figure 3.4, the 11 hz natural oscillations of the force balance can be seen in the unfiltered signals.

Only one channel of the time-dependent force output could be recorded due to hardware limitations. The lift output was chosen because specific aerodynamic characteristics could be more easily observed in the lift signal compared to the drag signal. In addition, the lift output had a higher signal to noise ratio than the drag output.

3.5 Flow Visualization

Various flow visualization techniques were needed to help determine the aerodynamic flow behavior of the airfoils in dry and wet conditions. Techniques were also developed to photograph the time-dependent water runback behavior to compare with the time-dependent lift output. Some observations were limited to the top surface of the airfoils. The suction surface of an airfoil has the more critical pressure distribution for aerodynamic performance, and so the top surface was always chosen since the tests were conducted mainly for positive lift cases. In addition, the bottom

surface was normally completely encompassed within the droplet impact zone which caused it to become completely wet immediately after rain initiation.

3.5.1 Video Photography

To help analyze the time-dependent output, a video camera was used to photograph the water runback behavior on the top surface of the airfoils. A photograph of the set-up is shown in figure 3.5.
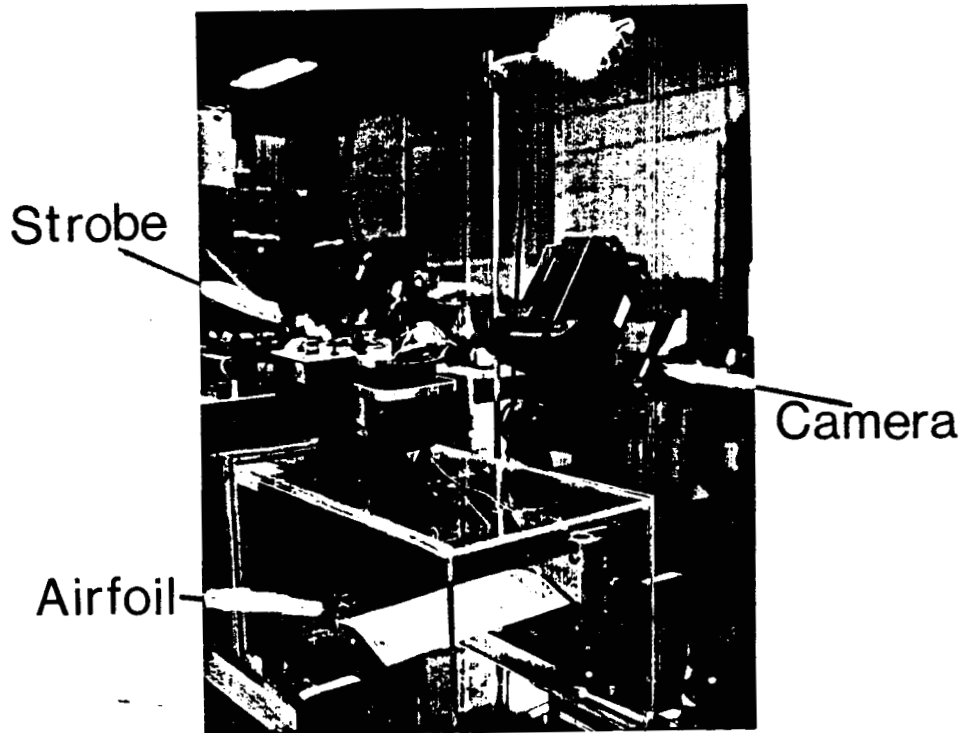
Figure 3.5. Photograph of the video photography set-up.

A strobe was synchronized with a Sony 8mm CCD video camera at the camera frame rate of 30 hz, to yield good frame by frame detail of the water runback behavior on the airfoil. With

53

only strobe illumination however, the photography became confused by the presence of high velocity freestream droplets in the foreground which were 'frozen' by the strobe effect. Therefore, overhead lights were also needed to produce useful photographs. A balance between the stroboscope and overhead lights was made to generate sharp frame by frame images, and yet still reduce the foreground water droplets. This video photography technique provided a valuable tool for correlating the time-dependent force output and actual water behavior on the airfoil.

3.5.2 Microtufts

In order to visualize boundary layer separation, microtufts were positioned on the top surface of the airfoils. However, the tufts become ineffective when wet. A technique was developed to protect the tufts in rain conditions and is shown in figure 3.6. The water runback pattern around the tufts was controlled by placing wax on the surface of the airfoil in a wedge pattern. The increased surface forces achieved at the wax interface makes the water runback avoid the waxed portion of the airfoil to keep the tufts dry for several seconds. This was sufficient time to observe changes in separation behavior on the airfoil in rain conditions. The microtufts had fluorescent properties and were exposed to ultra-violet light to enhance photographic quality.
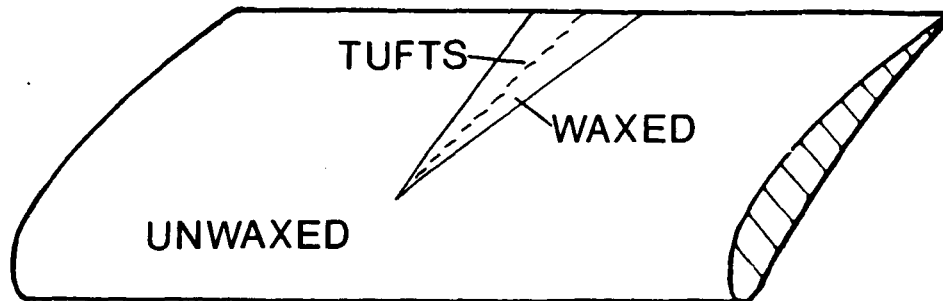
Figure 3.6. Schematic view of the tuft protection technique.

3.5.3 Liquid Crystals

In order to visualize boundary layer transition, liquid crystals[18] were applied to the top surface of the airfoils. The liquid crystals indicate variations in shear stress by color change. Due to the different shear stress found between laminar and turbulent boundary layers, laminar to turbulent transition can be seen as a distinct color discontinuity.

The presence of water over the liquid crystals prevented accurate observation of the color changes due to secondary optical effects. However, with the use of high speed video photography, the behavior of the boundary layer transition front prior to the development of water runback was observed. This produced adequate visualization of the transition phenomenon.

3.6 Computational Fluid Dynamics Code

To gain further insight into the boundary layer behavior and its effect on airfoil performance, a two-dimensional, compressible, viscid airfoil code was utilized[8,12]. The code predicts boundary layer behavior including laminar separation bubbles and reattachment points, boundary layer growth, and trailing edge separation. The code also allows the user to force boundary layer transition at a given location on the airfoil. The code was useful up to stall initiation, but had convergence problems at very high angles of attack due to the increasingly strong singularity which arises in the computational method as boundary layer separation strength increases. Input parameters for the CFD code included airfoil geometry, angle of attack, Reynolds number, Mach number, freestream turbulence level, and the boundary layer transition location when being specified by the user.

Chapter 4

RESULTS

4.1 Overview

The investigation of the performance degradation of airfoils in heavy rain conditions was conducted at a Reynolds number of 310,000 and equivalent rain rate of 1000 mm/hr. In general, two different mechanisms, causing performance degradation, were observed in these tests, and each occurred at different times after rain initiation. The first effect occurred immediately upon rain initiation and appeared to be the result of premature boundary layer transition from laminar to turbulent flow due to the water presence at the leading edge. The second effect occurred over longer time scales and appeared to be related to water runback behavior. The water layer is believed to effectively alter the airfoil geometry which results in an overall degradation of airfoil performance.

The results of the tests will be presented in this chapter as follows: In section 4.2, overall lift and drag curves comparing steady-state dry and wet performance for the three airfoils will be presented. In section 4.3, a comparison is made between the performance of the airfoils in dry and wet conditions with the performance of the airfoils when boundary layer transition is forced prematurely. In section 4.4, detailed time-dependent effects, flow

visualization data, and computation results will be presented for the airfoils at low angles of attack and then for high angles of attack in section 4.5. Finally, in section 4.6, airfoil surface/water contact angle effects on performance in wet conditions will be presented by comparison of waxed and unwaxed cases.

4.2 Steady-State Lift and Drag Force Data

Figures 4.1, 4.2, and 4.3 present lift and drag polar data for the Wortmann FX67-K170, the NACA 0012, and the NACA 64-210 airfoils in dry and wet conditions. At low angles of attack, all three airfoils show a decrease in lift and an increase in drag in rain conditions. However, the magnitude of the degradation varied significantly between the three airfoils. The Wortmann airfoil (figure 4.1) showed the greatest performance degradation. At low angles of attack, there is a reduction in slope and downward shift of the lift polar resulting in an overall lift coefficient reduction of approximately 25% due to rain. The maximum lift to drag ratio was reduced by 50%.

The NACA 0012 airfoil (figure 4.2) also had a reduction in the slope of the lift curve in wet conditions which corresponded to an overall reduction in lift of approximately 15% at low angles of attack. The corresponding loss in the maximum lift to drag ratio in rain conditions was approximately 30%.
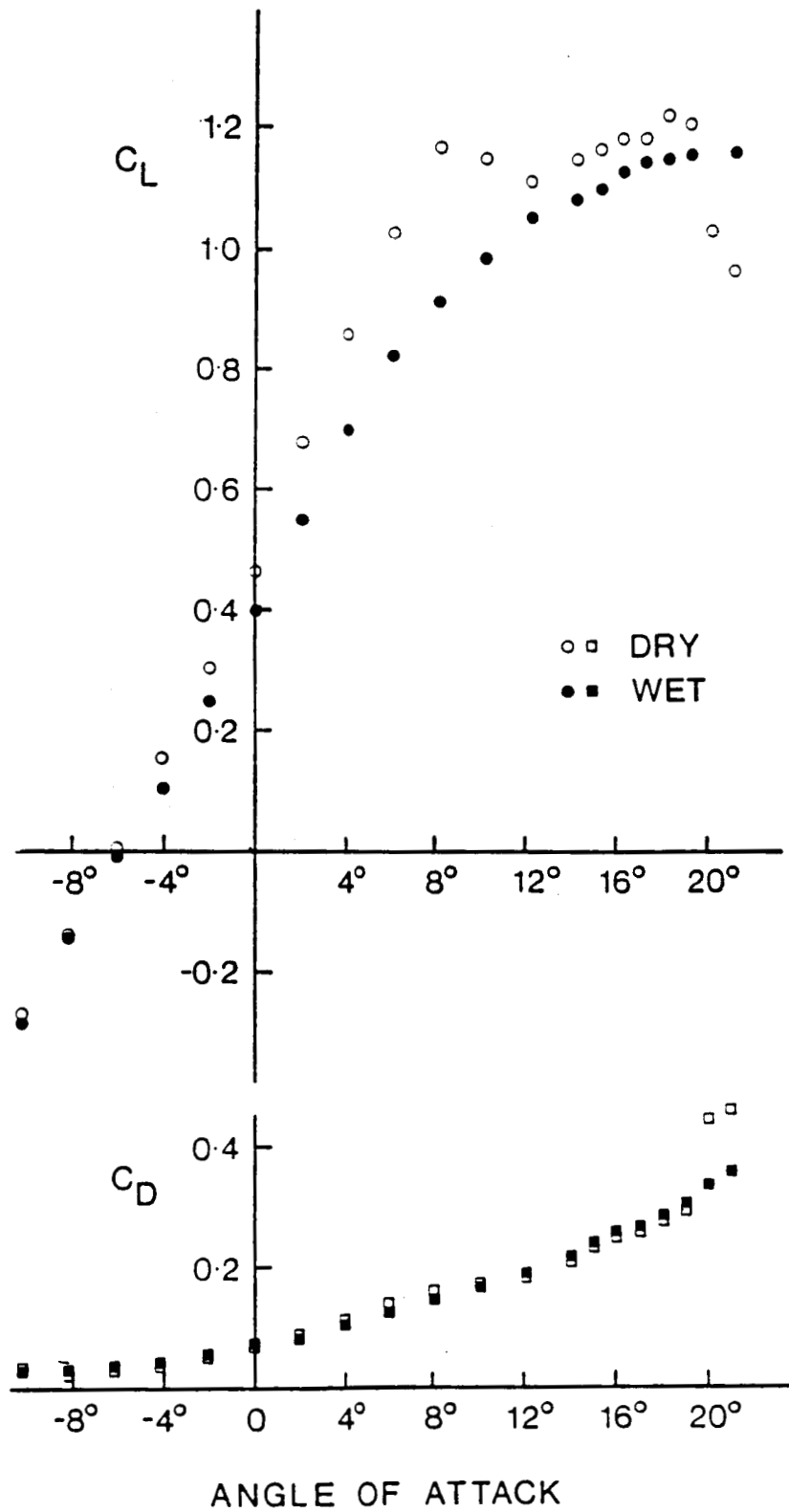
58

Figure 4.1. Lift and drag coefficient data vs. angle of attack for the Wortmann FX67-K170 airfoil in dry and wet conditions.
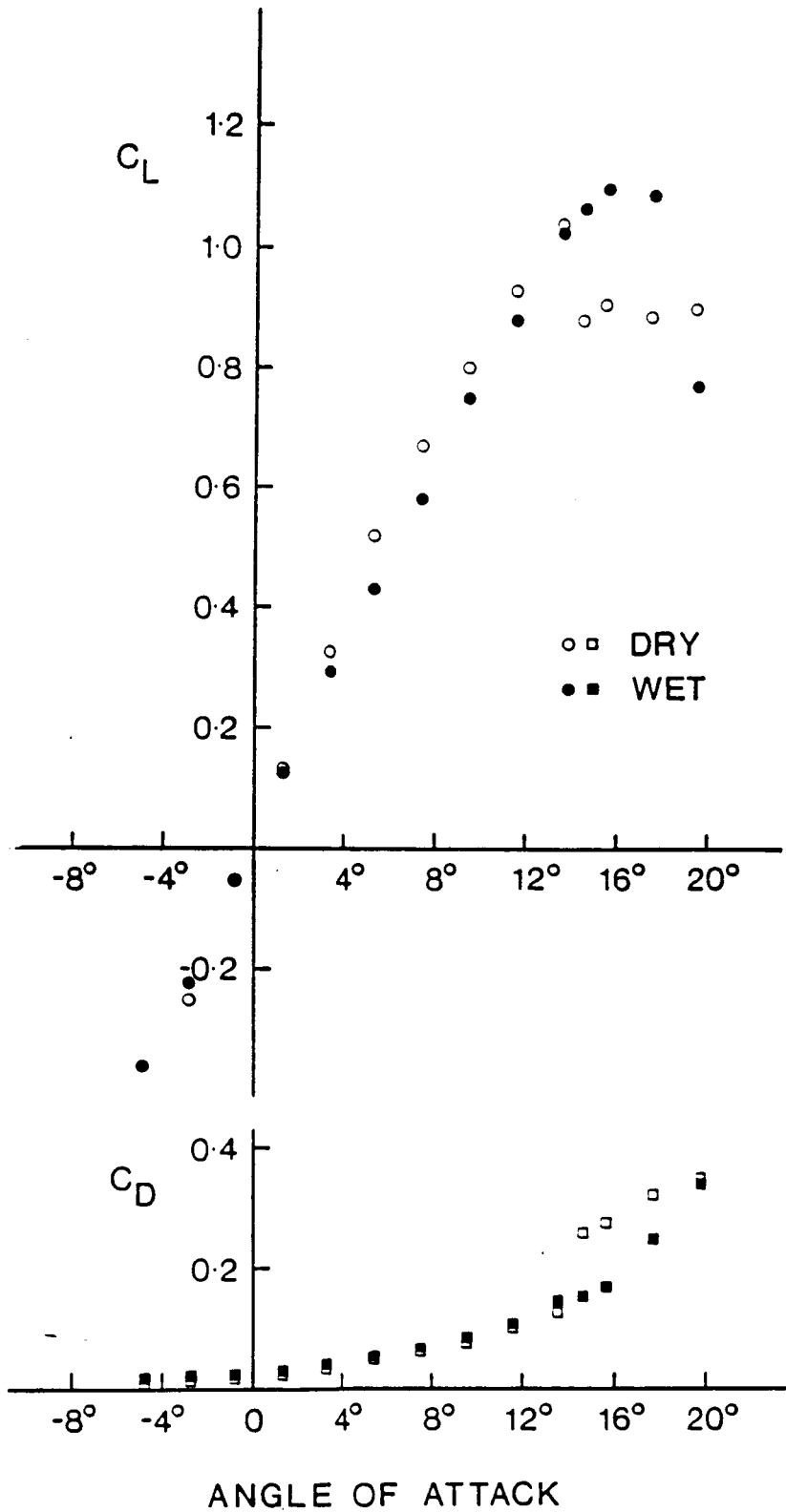
Figure 4.2.   Lift and drag coefficient data vs. angle of attack for the NACA 0012 airfoil in dry and wet conditions.

60
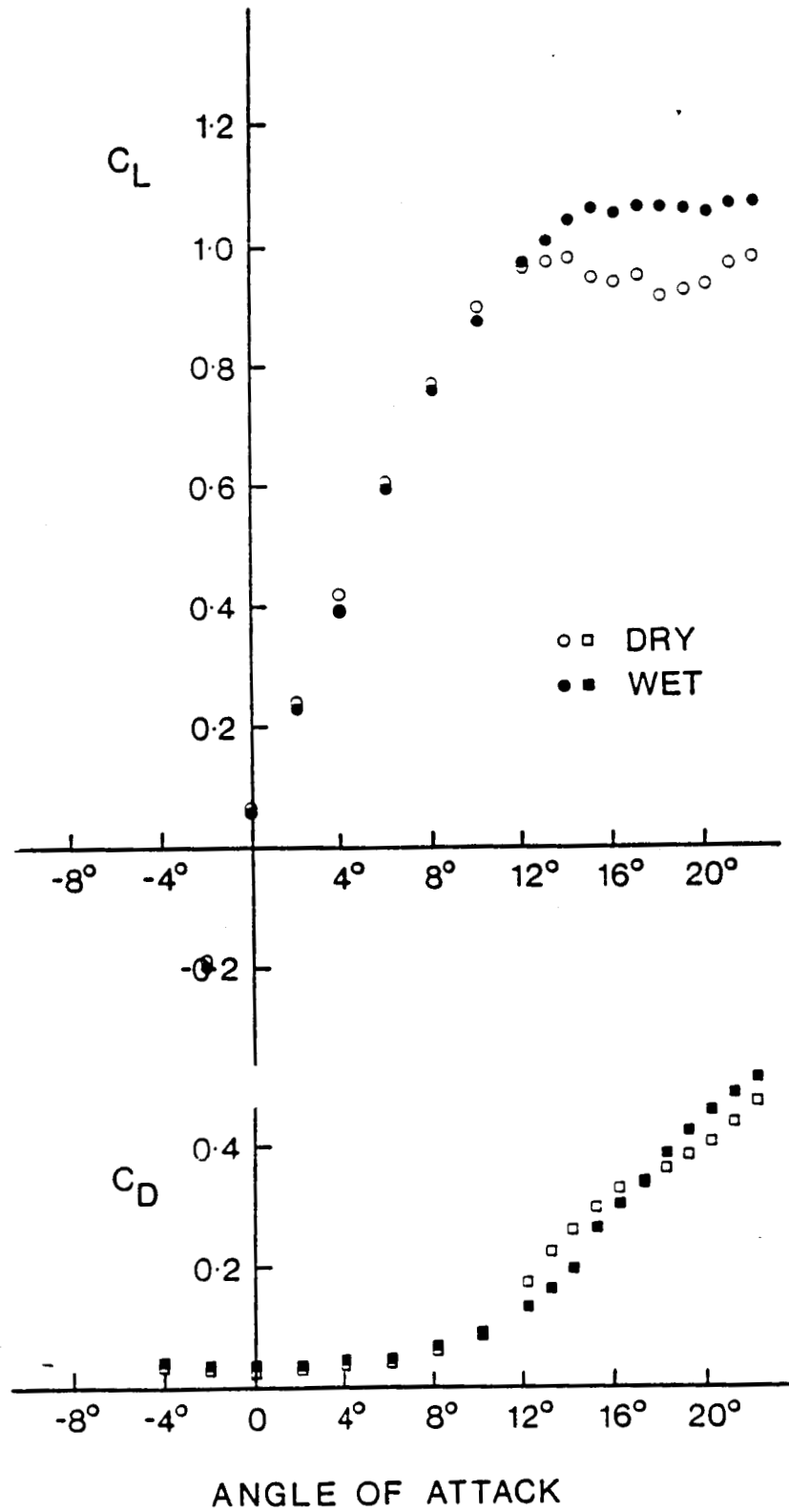
Figure 4.3. Lift and drag coefficient data vs. angle of attack for the NACA 64-210 airfoil in dry and wet conditions.

The NACA 64-210 airfoil (figure 4.3) had minimal lift degradation in heavy rain conditions, but due to an increase in drag, the maximum lift to drag ratio was reduced by approximately 20%.

Generally, all three airfoils had an overall increase in drag of around 20% in wet conditions at low angles of attack. The drag increase can be partially attributed to the droplet momentum transfer. Using equation 2-11, an upper limit estimate of approximately 0.010 on the drag coefficient increase due to droplet impact is calculated. This increase is of the same order of magnitude as the increase in drag measured near minimum drag angles of attack for all three airfoils. Therefore, the drag increase due to the droplet momentum transfer in wet conditions appears to be fairly important. However, other effects are probably also important, and decoupling all the potential performance degrading mechanisms in the drag data is difficult.

At high angles of attack above stall initiation, the effect of rain was varied. Both the NACA 0012 (figure 4.2) and NACA 64-210 (figure 4.3) airfoils exhibited an unexpected performance enhancement in this regime. The stall angle for the NACA 0012 airfoil was increased from 14° in dry conditions to 18° in wet conditions. For the NACA 64-210 airfoil, stall initiation occurred at approximately the same angle of attack in both dry and wet conditions (12°). However, for the wet case, the NACA 64-210 airfoil had

increased performance in stall conditions compared to the dry case.

At high angles of attack, the lift polar for the Wortmann airfoil (figure 4.1) in dry conditions was erratic indicating the presence of a complicated stall process which is thought to be related to the low Reynolds number boundary layer behavior. In wet conditions however, the lift polar of the Wortmann was much smoother but had a decrease in performance compared to the dry behavior.

The varied susceptibility of the airfoils to heavy rain appears to be related to the natural boundary layer regime with which the airfoils are designed to operate. The Wortmann airfoil is designed to have a laminar boundary layer over at least 50% of the chord for high efficiency. In the presence of rain, the boundary layer is thought to transition prematurely, and hence, the performance of the Wortmann airfoil suffers significant losses. In contrast, the NACA 64-210 airfoil is designed to operate with a fully turbulent boundary layer. Therefore, when the airfoil is tested in wet conditions, only minor performance losses are measured which are consistent with the susceptibility of the airfoil to premature boundary layer transition. The NACA 0012 airfoil had intermediate performance degradation in rain conditions which may indicate that the aerodynamic efficiency of this airfoil is increased by the presence of an extended region of laminar flow.

4.3 Tripped Boundary Layer Results

Previous wind tunnel experiments performed by Hansman and Barsotti[16] suggest that premature boundary layer transition caused the aerodynamic performance losses measured for natural laminar airfoils at low Reynolds numbers in heavy rain conditions. To investigate this hypothesis, boundary layer transition elements were placed on the suction and pressure surfaces of each airfoil. Trip strips that were 0.635 cm (0.25 inches) wide and made up of sand grains ranging in diameter from 0.635 mm to 1.016 mm were placed at the 5%, 25%, 50%, or 75% chordwise station on the top and bottom surface of each airfoil. Trip strips on the lower surface of the airfoils resulted in minimal performance changes whereas forcing boundary layer transition on the upper surface resulted in fairly significant performance changes. Therefore, the location of the lower trip strip location was generally fixed at 5% chord and the upper trip strip location was varied.

Results of the forced boundary layer transition tests are shown in figures 4.4, 4.5, and 4.6. For each airfoil, the trip strip position that best models the wet behavior is shown. However, this does not necessarily imply that transition does occur at these specific locations in wet conditions. It merely indicates the ability to model the wet behavior with trip strips at some location on the airfoil.

64

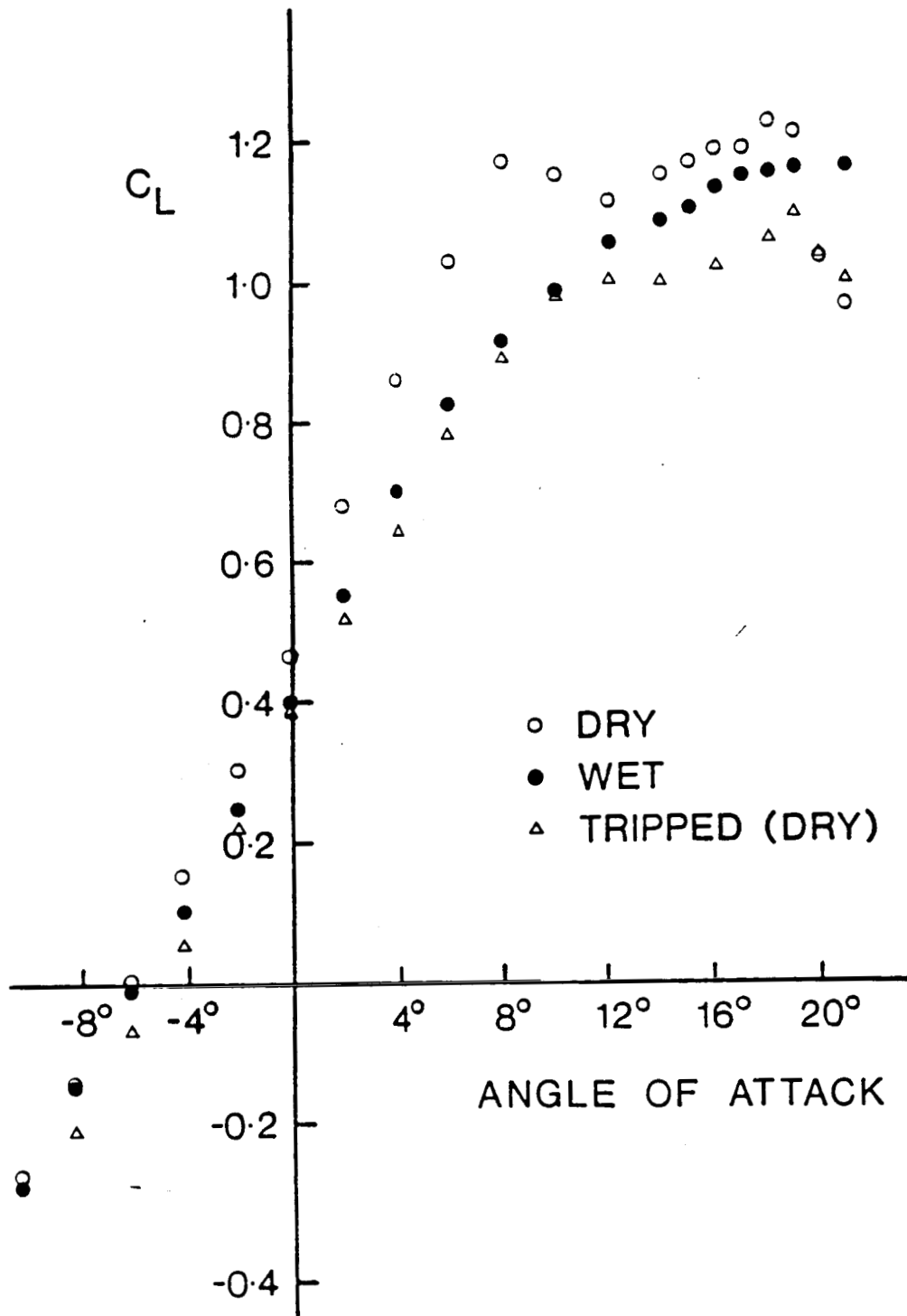Figure 4.4. Comparison of the dry, wet, and tripped boundary layer (25% chord, top surface) lift polars for the Wortmann FX67-K170 airfoil.
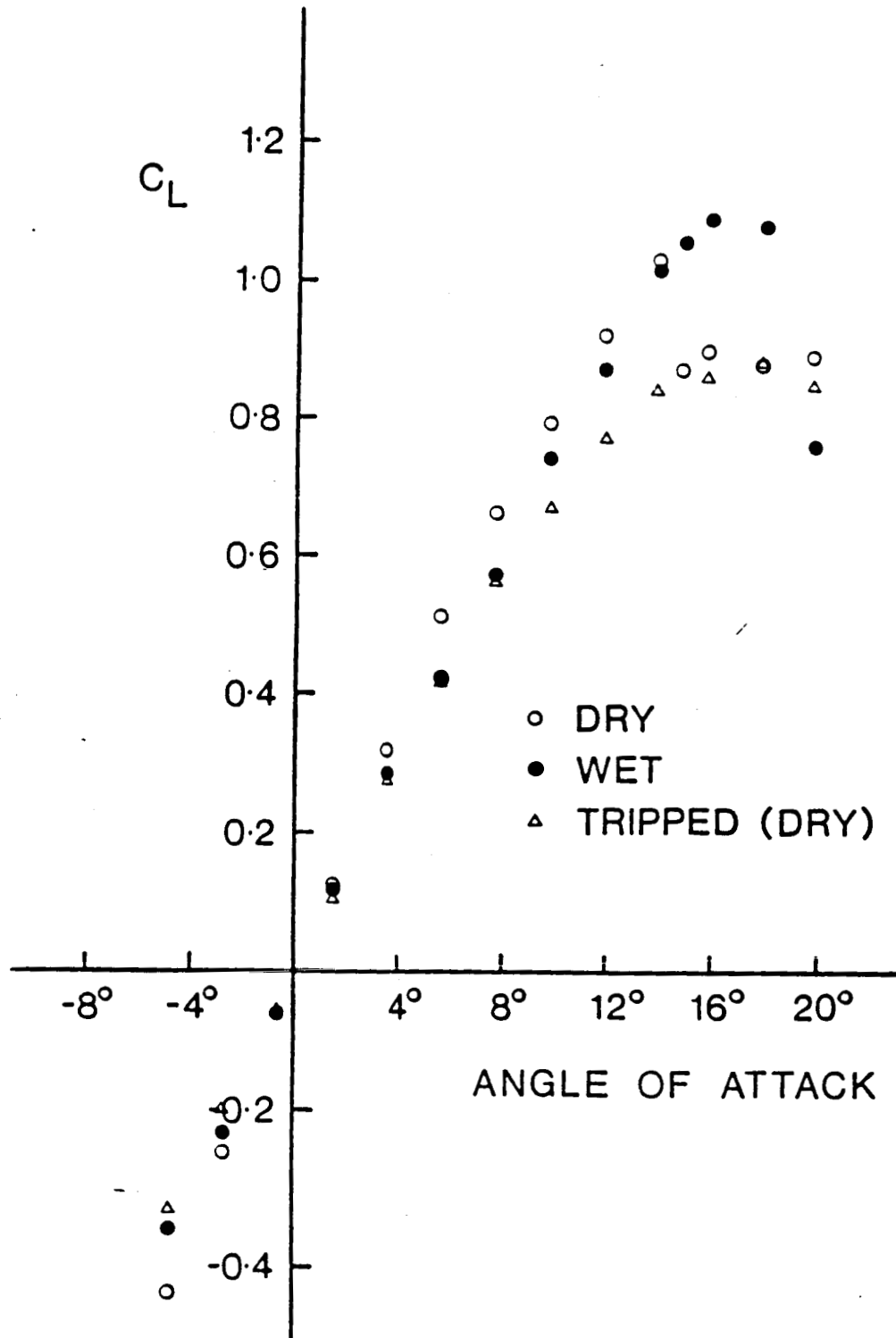
Figure 4.5. Comparison of the dry, wet, and tripped boundary layer (5% chord, top surface) lift polars for the NACA 0012 airfoil.
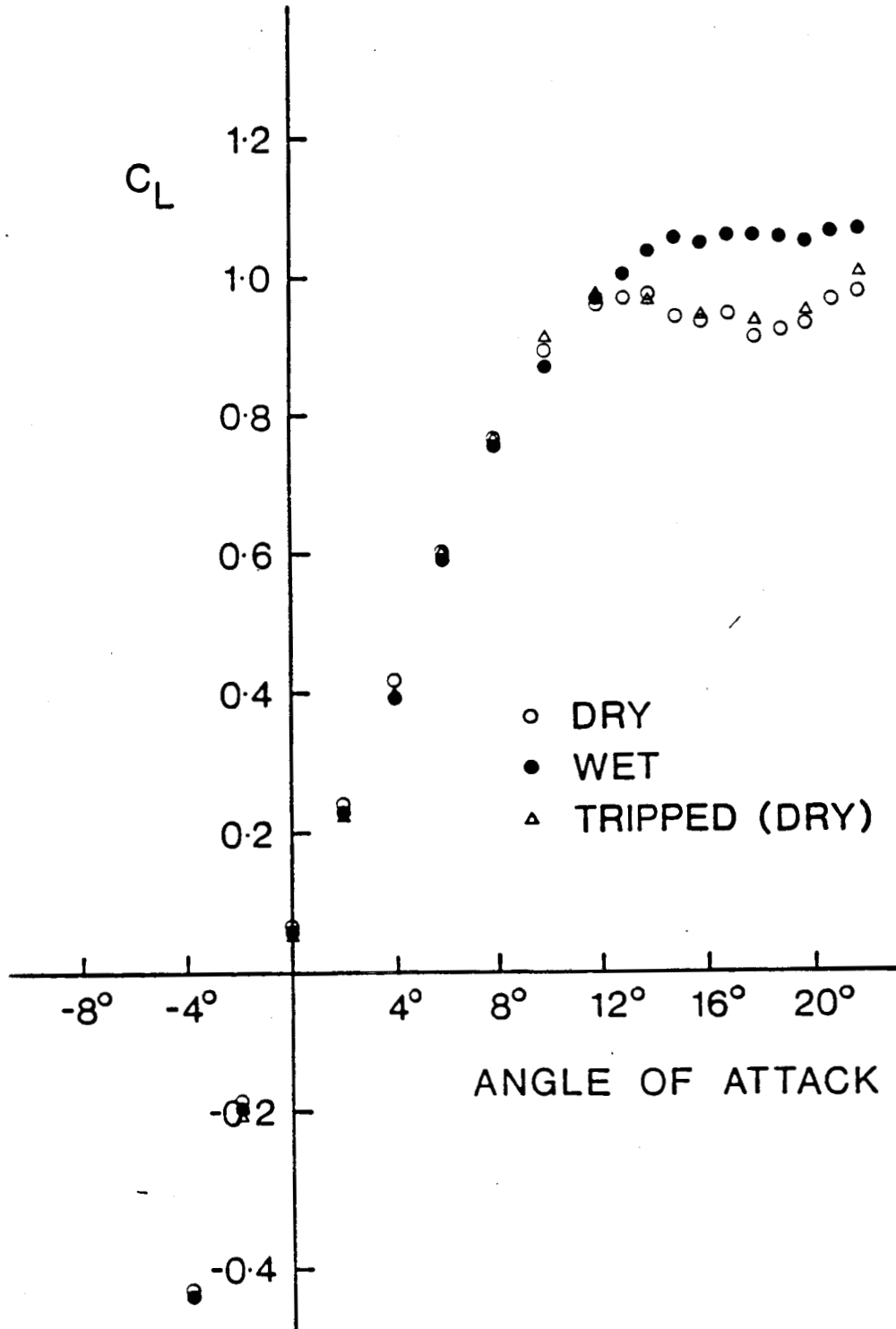
Figure 4.6. Comparison of the dry, wet, and tripped boundary layer (5% chord, top surface) lift polars for the NACA 64-210 airfoil.

For the NACA 0012 (figure 4.5) and the NACA 64-210 (figure 4.6) airfoils, trip strips at 5% chord on the top surface best modeled the wet conditions. The performance of the Wortmann airfoil (figure 4.4) in wet conditions was best emulated with trip strips placed at 25% chord on the top surface. When transition was forced at 5% chord on the upper surface of the Wortmann airfoil, the performance measured became considerably worse than the observed performance of the airfoil in wet conditions. The favorable pressure gradient which extends to approximately 40% chord for the Wortmann airfoil may act to decrease the instability growth rate in the boundary layer. This would delay transition even in wet conditions on this airfoil and explain the successful wet performance emulation by roughness at 25% chord. However, the aft position of the transition emulation point (25% chord) for the Wortmann airfoil may also be an indication that the sand grain size used in these tests is too large to emulate the water roughness, and so excessive degradation is observed when the grains are placed at 5% chord.

In general, the magnitude of the low angle of attack airfoil performance degradation in wet conditions could be emulated well by placing trip strips near the leading edge of each of the airfoils. However, the high angle of attack behavior of the NACA 0012 (figure 4.5) and NACA 64-210 (figure 4.6) airfoils could not be emulated by these

elements. The trip strip location at 5% chord may have been aft of the high angle of attack leading edge separation point for these two airfoils as depicted in figure 4.7. This would explain the unsuccessful attempts to emulate the high angle of attack wet behavior with trip strips. However, the overall ability to model the heavy rain performance degradation at low angles of attack with trip strips suggests that the low angle of attack aerodynamic degradation measured in heavy rain is caused by a premature boundary layer transition mechanism.

S

Trip Strip Location
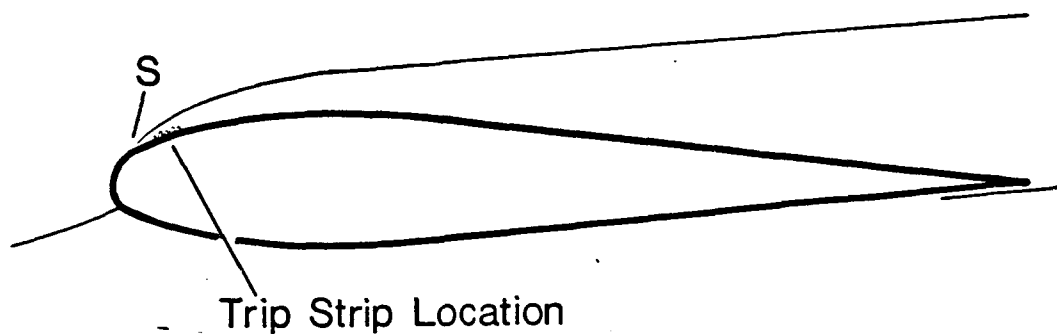
Figure 4.7. Example of a trip strip positioned aft of a leading edge separation point.

4.4 Low Angle of Attack Behavior

In order to better understand the mechanisms resulting in performance degradation in heavy rain, time-dependent lift force output was recorded at low angles of attack and correlated with video observations of the water runback behavior on the upper surface of the airfoils. Visualization was limited to the upper surface because the upper surface was found to be the more critical surface in boundary layer trip tests. Also, the lower surface was generally observed to quickly become completely wet at most angles of attack.

The Wortmann airfoil had the most significant performance degradation at low angles of attack, and therefore, its results will be presented first and in greatest detail. The primary mechanism which caused performance degradation in wet conditions at low angles of attack occurred immediately upon rain initiation and appeared to be associated with a boundary layer transition phenomenon. A secondary effect occurred at longer time scales consistent with the top surface water runback time. The associated degradation appeared to be caused by the water layer which seems to effectively alter the airfoil geometry.

4.4.1 The Wortmann FX67-K170 Airfoil

Figure 4.8 shows the time-dependent lift output and water runback position for the Wortmann airfoil at 2° angle of attack.
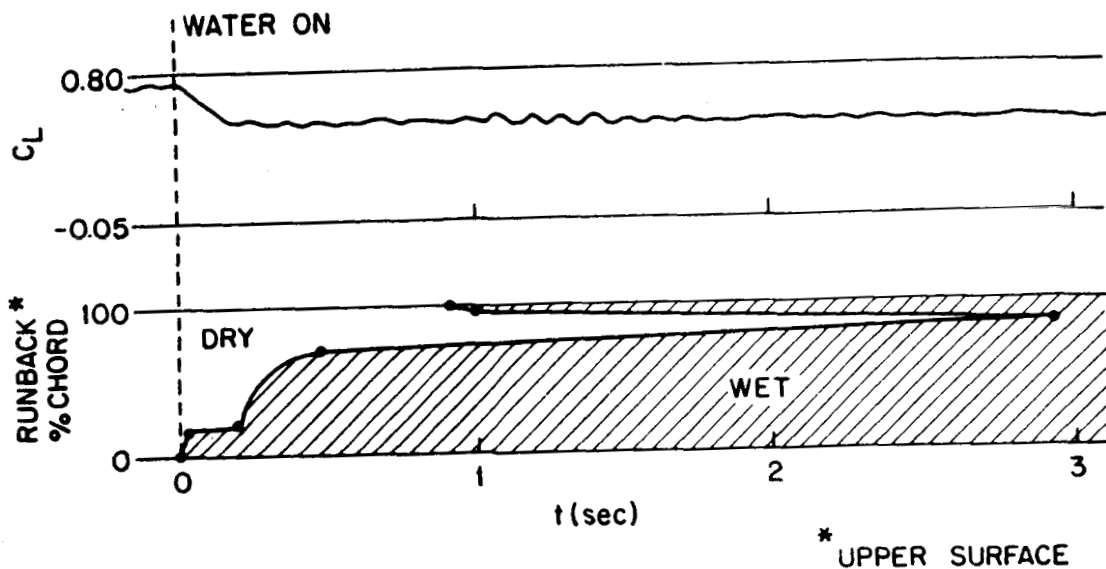
Figure 4.8. Time-dependent lift and water runback position for the Wortmann FX67-K170 airfoil at 2° angle of attack.

The water runback graph indicates the average position of the runback front with respect to time after rain is initiated. Photographs of the top surface water runback pattern are shown in figure 4.9 to illustrate typical spanwise variations in the water runback development which are not indicated in the water runback graph. The arrows in figure 4.9 indicate the position of the rivulet runback front which is graphed in figure 4.8. Spanwise variations in the runback front position were generally less than 15% chord.

In addition, it should be noted that even though the runback graphs appear to indicate the time needed to reach a quasi-steady, fully developed water distribution on the airfoil, this may not be the case. Additional water layer thickening and spanwise movement of the water runback may still be occurring even after the airfoil is wet from 0% to

71
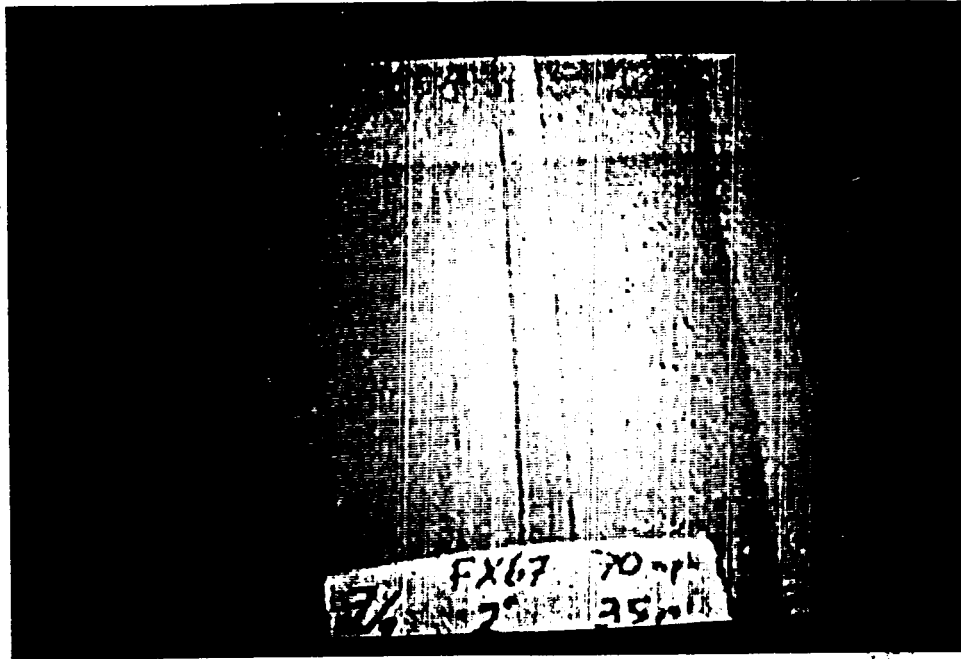
.33 sec

V_∞
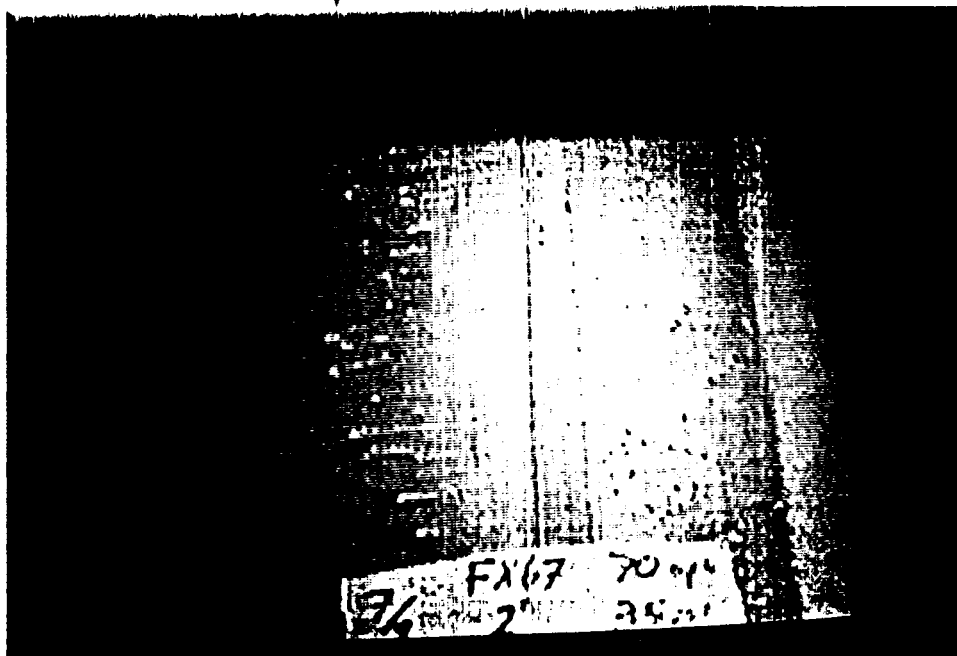
.66 sec

Figure 4.9-1.   Photographs of the water runback behavior at
    various times since rain initiation for the Wortmann
    FX67-K170 airfoil at 2° angle of attack.   The arrows
    indicate location of runback front plotted in figure 4.8.

72

1.17 sec

V_∞
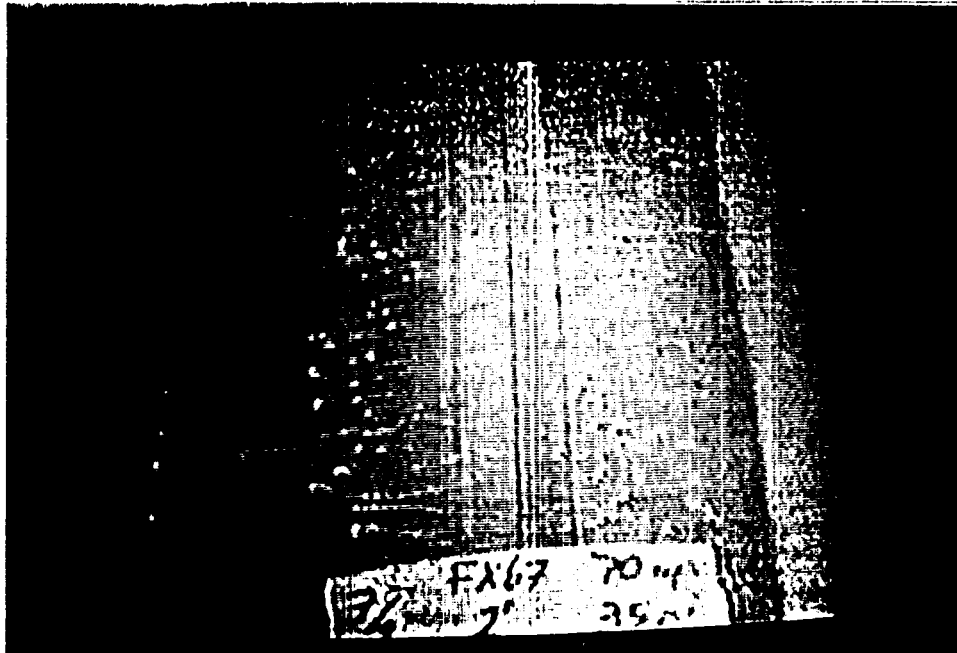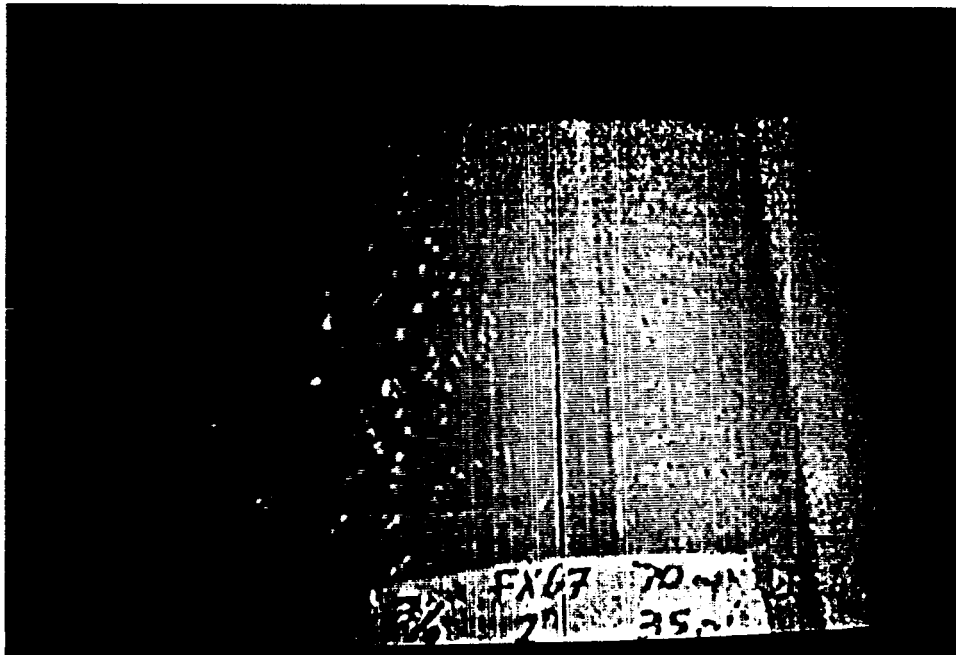
3.0 sec

Figure 4.9-2. Photographs of the water runback behavior at
   various times since rain initiation for the Wortmann
   FX67-K170 airfoil at 2° angle of attack. The arrows
   indicate location of runback front plotted in figure 4.8.

73

100% chord.   The runback graph merely indicates the typical time scales associated with the water runback behavior.

In some cases, water appeared at the trailing edge and progressed forward.   This can be seen in figure 4.8 at approximately 0.9 seconds.   This phenomenon is an indication of a trailing edge separation and flow reversal which forces water from the lower surface around the trailing edge to the upper surface.

In the lift coefficient data of figure 4.8, two distinct time scale effects are present.   Initially (within the first 0.2 seconds), there is a significant loss of lift.   This time scale is consistent with the response of the experimental force balance to a step input (0.1 seconds at 10 hz) and is the same order of magnitude (approximately 10 advection chord lengths) as the unsteady time scale found for an airfoil that encounters a sudden gust or undergoes a sudden change in angle of attack[4].   At this point, the water is only present near the leading edge at less than 20% chord.   This rapid loss of lift appears to be resulting from premature transition of the boundary layer induced by the water at the leading edge.

This hypothesis was confirmed by liquid crystal observations.   In dry conditions, the liquid crystals indicated boundary layer transition at approximately the 65% chord station as shown in figure 4.10.   Within 1/30 of a second after rain initiation, the boundary layer transition

V_∞
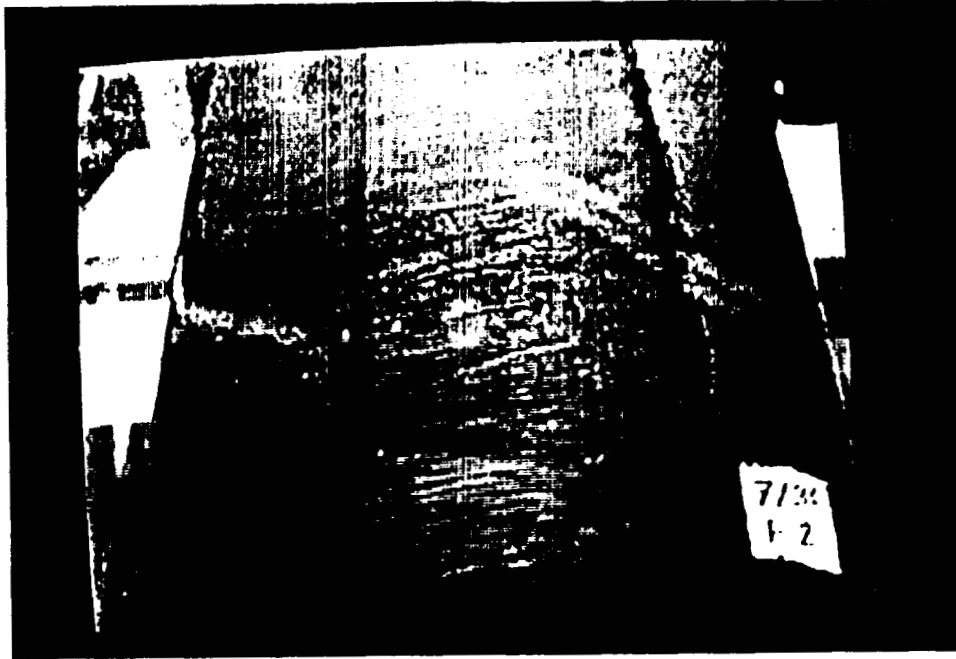
Figure 4.10. Liquid crystal boundary layer visualization
   results for the Wortmann FX67-K170 airfoil at 2° angle of
   attack in dry conditions. The arrow indicates the boundary
   layer transition front position as indicated by the liquid
   crystals.

point moved to within 20% of the leading edge as indicated by

the crystals with the video photography. The water layer

extended to 20% chord, so the exact location of the boundary

layer transition point is not known. However, it is likely

that the transition from is ahead of the 20% chord point.

The CFD code likewise predicted boundary layer

transition at 65% chord in dry conditions at a Reynolds

number of 310,000. Figure 4.11 shows the CFD results for the

Wortmann airfoil at 2° when boundary layer transition is

allowed to occur naturally and when it is forced near the

leading edge. Separation, transition, reattachment, and

natural conditions

FX 67-K-170
MACH = 0.100
RE   = 0.300 × 10⁶
ALFA = 2.000
CL   = 0.7027
CD   = 0.01465
CM   = -0.1020
L/D = 47.98

(a)

forced conditions

FX 67-K-170
MACH = 0.100
RE   = 0.300 × 10⁶
ALFA = 2.000
CL   = 0.4942
CD   = 0.02309
CM   = -0.0794
L/D = 21.41

(b)
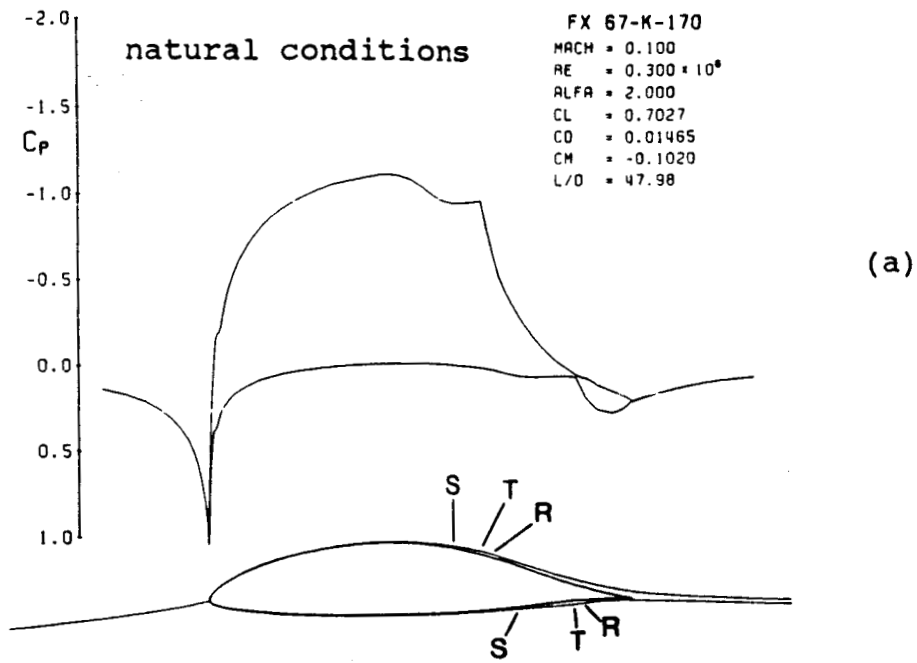
Figure 4.11.   Computer generated flow field and pressure
distribution for the Wortmann FX67-K170 airfoil at 2° angle
of attack for natural transition (a) and forced transition
(b) cases.   Boundary layer Separation, Transition,
Reattachment, and Forced Transition locations are indicated
by S, T, R, and FT respectively.

76

forced transition are indicated in the figures by the letters S, T, R, and FT respectively. In figure 4.11a, natural transition is caused by a laminar separation bubble at 65% chord. In figure 4.11b, transition is forced at the 5% chord station because from the trip strip experiments, rain appeared to induce transition in this region, although this choice is somewhat arbitrary. The resulting decrease in the lift coefficient was approximately 0.21 from the natural case to the forced case in the CFD code, and 0.14 from the dry to the wet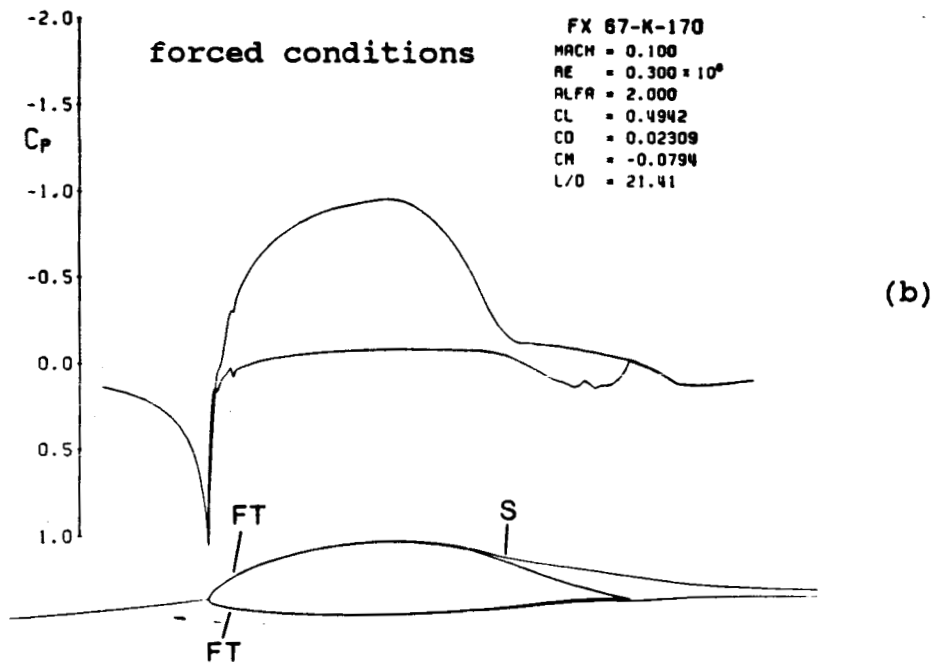 conditions in the experimental data (figure 4.1). This agreement is fairly good, and the additional lift degradation predicted by the CFD code may indicate that transition occurs aft of the 5% chord location for the Wortmann airfoil in rain conditions.

Another phenomenon apparent in the water behavior at low angles of attack for the Wortmann airfoil is a trailing edge separation present in the rain conditions. At about 0.9 seconds, water is seen to be drawn from the lower surface to the upper surface at the trailing edge of the airfoil as indicated in figure 4.8. As observed in video data, the water layer in the region from 80% chord to the trailing edge moved very slowly and thickened considerably compared to the water layer forward of the 80% chord location. This indicates that boundary layer separation is occurring at approximately 80% chord. The CFD code also predicted a trailing edge separation at approximately 80% chord when

transition was forced at 5% chord (figure 4.11b). In dry boundary layer conditions, no trailing edge separation was predicted by the code (figure 4.11a) and none was observed in tuft studies of the airfoil. These results are consistent with other studies which indicate that a trailing edge separation is not uncommon when an airfoil's boundary layer is transitioned prematurely[9].

After the initial lift loss on the Wortmann airfoil, a small additional performance loss occurred at time scales consistent with the full chord water runback time (0.2 to 3.0 seconds in figure 4.8). After that time, no future gross changes in the lift are seen. This behavior is observed for each of the airfoils at low angles of attack where there is a lift change associated with the runback time scale.

The longer time scale effects normally acted to decrease airfoil performance. However, in some cases, the lift in the time-dependent output was observed to increase over the longer time scales after the initial losses. This phenomenon is shown in figure 4.12 for the Wortmann airfoil at -4° angle of attack. An increase in lift over longer time scales was fairly infrequent and normally occurred at angles of attack near zero lift.

The longer time scale lift changes associated with the water runback behavior do not appear to be a result of the additional distributed roughness which is generated as the water layer develops. The roughness at the leading edge
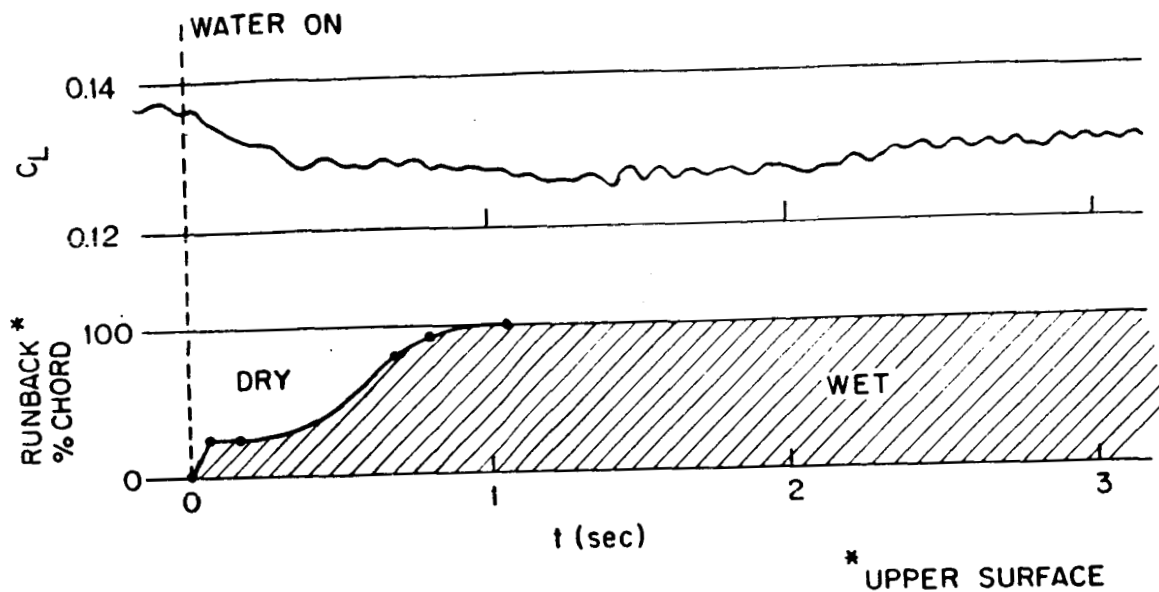
Figure 4.12. Time-dependent lift and water runback position
   for the Wortmann FX67-K170 airfoil at -4° angle of attack.

initiates the transition effects, and the additional
roughness associated with the water runback behavior should
not significantly alter this mechanism. Although the
additional distributed roughness probably results in some
additional performance degradation, the most important
mechanism seems to be an effective airfoil geometry change
due to the water runback layer presence. The water layer
generally induced a decrease in performance by altering the
effective airfoil geometry. However, the water layer may
become distributed in such a way to increase airfoil
performance (figure 4.12).

It should be noted that because of the small scales
employed in these experiments, the ratio of the water layer
thickness to chord length is artificially high. Therefore,
as described in section 2.3.5, the significance of the water

79

runback layer effects is likely enhanced in these small scale
tests, and care should be exercised when extrapolating these
particular results to full scale applications.

4.4.2 The NACA 0012 Airfoil

Figure 4.13 shows the time-dependent output for the NACA
0012 airfoil at 2^O angle of attack.   The magnitude of the
lift degradation is less than for the Wortmann airfoil at 2^O
angle of attack, but the mechanisms appear the same.   There
is an immediate loss of lift initially, related to the
boundary layer transition mechanism as well as a slower,
secondary degradation correlated with the water runback
behavior.   Both these effects are seen in the time-dependent
lift output, and the long time scale effects are consistent
with the water runback time scales.
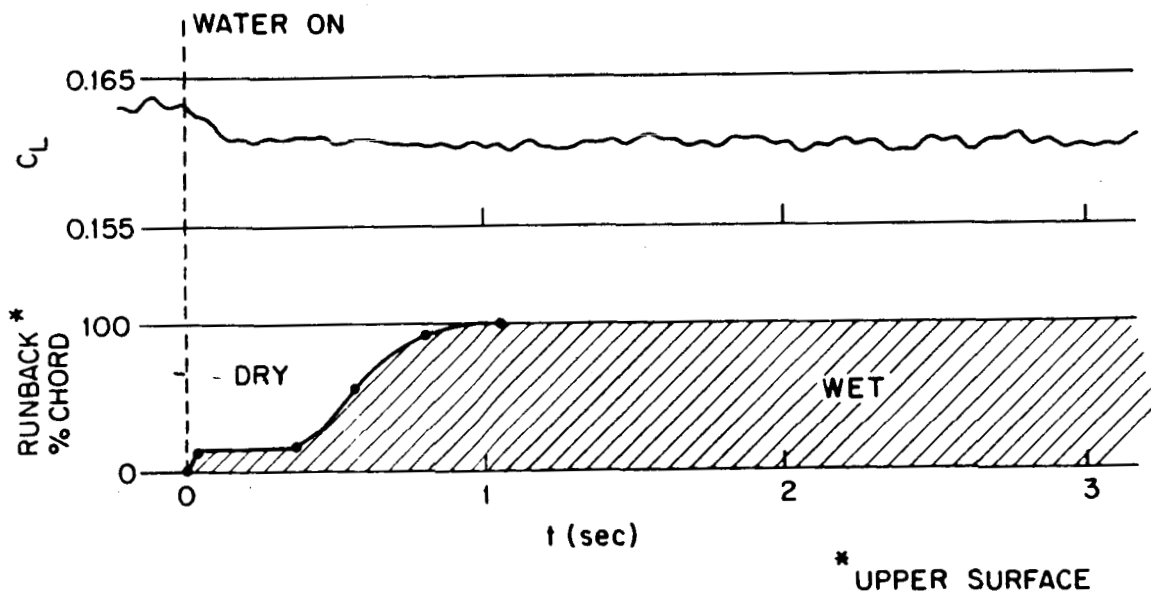
Figure 4.13.   Time-dependent lift and water runback position
for the NACA 0012 airfoil at 2^O angle of attack.

The CFD code was again used to predict aerodynamic performance and boundary layer behavior for the NACA 0012 airfoil at 2° angle of attack. For the natural transition case, the CFD code predicts boundary layer transition at about 55% chord, indicating a fairly significant laminar flow portion. When transition is forced at the leading edge in the CFD code, the lift coefficient decrease (~ 0.01) is consistent in magnitude to the degradation measured between dry and wet conditions (~ 0.01, figure 4.2). No trailing edge separation resulting from premature boundary layer transition was indicated for this airfoil at 2° angle of attack by either experimental or computational methods.

4.4.3 The NACA 64-210 Airfoil

The time-dependent output for the NACA 64-210 airfoil at 1° angle of attack is shown in figure 4.14. The time-dependent lift behavior differs from the NACA 0012 or Wortmann airfoils. The relative importance of the initial lift degradation is small compared to the degradation observed at longer runback time scales. The magnitude of the total change in the lift coefficient for the NACA 0012 airfoil (figure 4.13) and the NACA 64-210 airfoil (figure 4.14) is nearly equivalent. However, the NACA 0012 losses occur mainly in the first 0.15 seconds while the NACA 64-210 losses occur over a longer time scale (approximately 2 seconds).

81
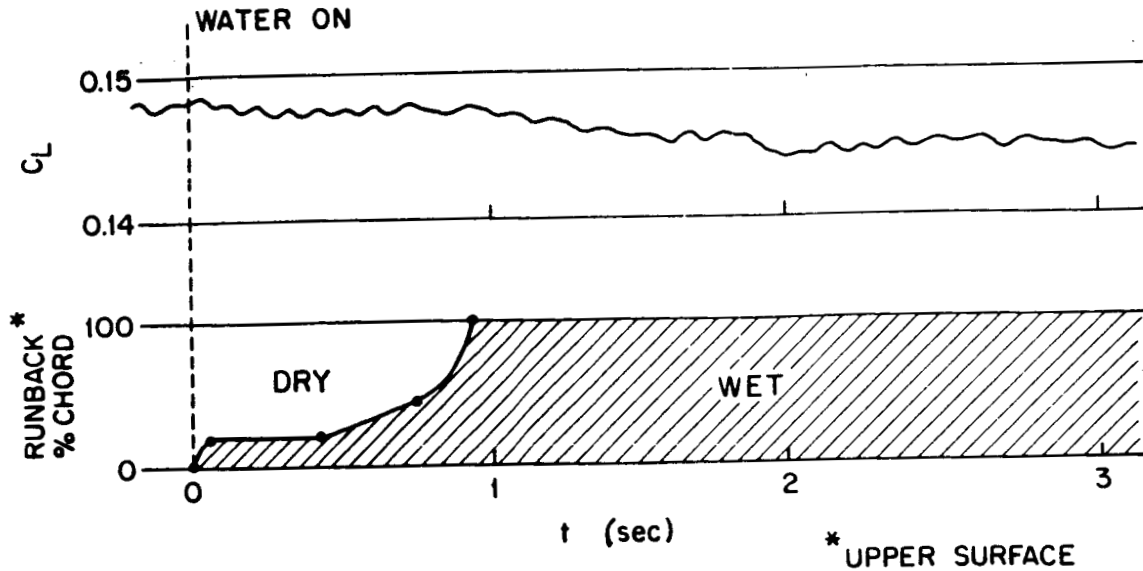
Figure 4.14. Time-dependent lift and water runback position for the NACA 64-210 airfoil at 1° angle of attack.

Both liquid crystal observations and the CFD code indicate boundary layer transition occurs at about 75% chord for the NACA 64-210 airfoil at 1° angle of attack in dry conditions. When transition is forced at the leading edge in the CFD code, the lift coefficient degradation (~ 0.01) is again consistent in magnitude to the experimental results (~ 0.01, figure 4.3). However, the premature transition mechanism developed in rain conditions is thought to be unimportant for the NACA 64-210 airfoil, so the agreement between the CFD and experimental results is not significant.

One additional general observation for the NACA 64-210 airfoil is that less water was present on the top airfoil surface. This caused the water rivulets to breakup into individual drops that would then runback at higher

velocities.   This effect resulted in increased runback velocities aft of the rivulet break up location of 50% chord as seen in figure 4.14.   This behavior is most likely caused by local collection efficiency effects (section 2.3.2) resulting from the thin airfoil section and small leading edge radius of curvature.

4.5 High Angle of Attack Behavior

The steady-state output of the airfoils at high angles of attack appeared significantly different from low angle of attack behavior (figures 4.1, 4.2, 4.3).   The methods used to analyze the heavy rain effects at high angles of attack are similar to those discussed above for low angles of attack. However, due to convergence problems resulting from the presence of strongly separated regions at high angles of attack, the CFD code could not be used in this regime.

The NACA 64-210 airfoil showed the most unexpected high angle of attack behavior in rain conditions (figure 4.3). It was, therefore, studied in greatest detail at high angles of attack, and its results will be presented first.

4.5.1 The NACA 64-210 Airfoil

At high angles of attack, the NACA 64-210 airfoil exhibited increased lift and decreased drag in wet conditions (figure 4.3).   This behavior was unexpected, and further experiments were executed in an attempt to identify the

mechanisms generating these increases in performance.

Time-dependent lift output is shown in figure 4.15 for the NACA 64-210 airfoil at 15° angle of attack. The lift increase occurs within 0.3 seconds after rain initiation. At this time, the water layer is only present in the first 10% of the chord as seen in the runback graph. This indicates that a leading edge phenomenon is causing the performance enhancement. In fact, top surface water runback on the airfoil did not begin until about 2 seconds after the rain was initiated (figure 4.15), and it developed at the trailing edge due to the separated flow.
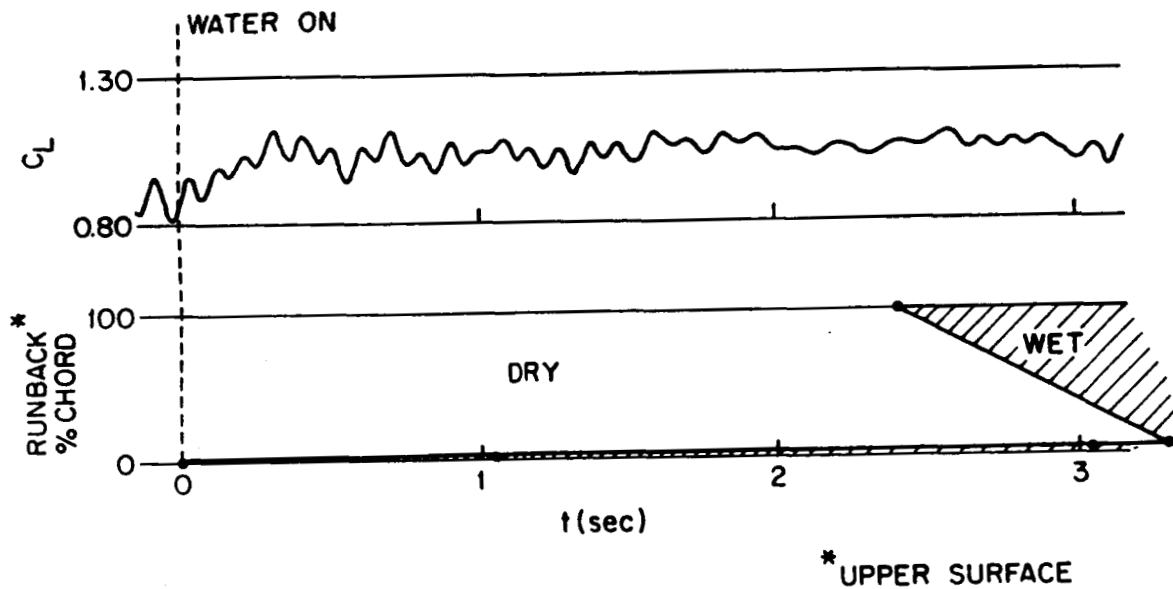
Figure 4.15. Time-dependent lift and water runback position for the NACA 64-210 airfoil at 15° angle of attack.

Top surface separation behavior was observed for the NACA 64-210 airfoil at 12° angle of attack in dry and wet conditions by microtufts as shown in figure 4.16. In dry

84

(a) dry

V_∞
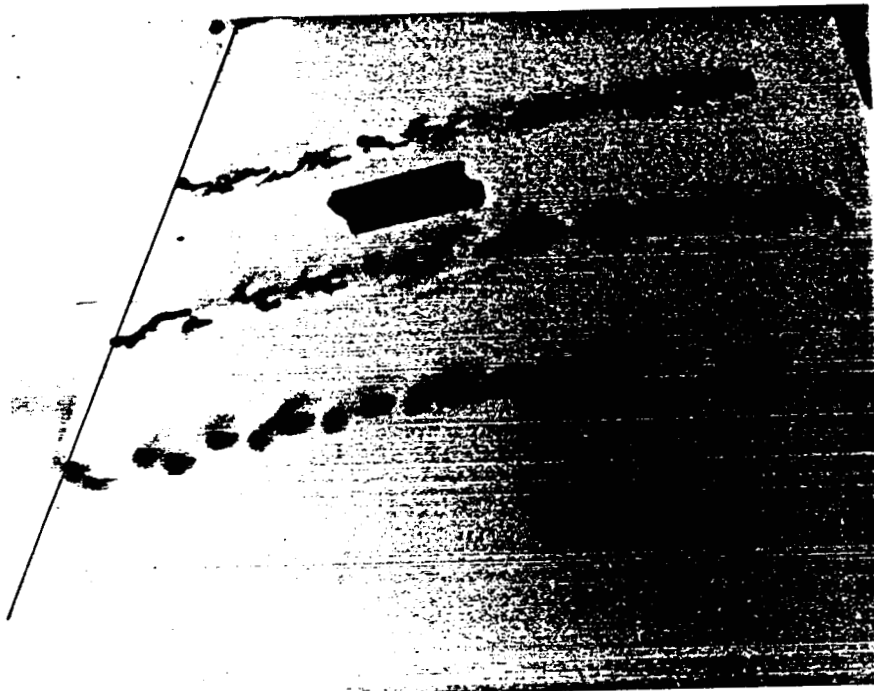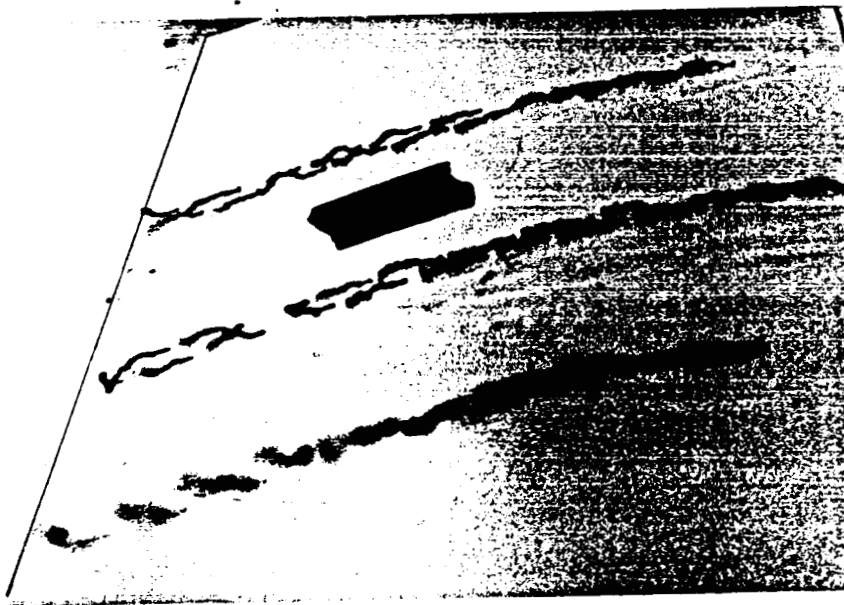
(b) wet

Figure 4.16.   Dry (a) and wet (b) separation behavior shown
   by microtufts for the NACA 64-210 airfoil at 12° angle of
   attack.

85

conditions (figure 4.16a), the microtufts are flapping and pointed into the flow direction which indicates the presence of a severe leading edge separation. In the wet condition (figure 4.16b), however, the tufts are laying steady, forward of the 50% chord location, which indicates that the leading edge separation has been reduced. The separation behavior was observed to change immediately upon rain initiation, prior to any wetting effects of the tufts.

The mechanism which decreases the stall severity at higher angles of attack in wet conditions is thought to be caused by a premature transition phenomenon. The rain presence is believed to roughen the surface, inducing boundary layer transition, resulting in increased mixing and an energized boundary layer. This allows the boundary layer to remain attached farther aft on the airfoil which results in an increase in performance.

The increased performance of the NACA 64-210 airfoil at high angles of attack appears to be caused by premature transition, but this phenomenon was not emulated by the trip strip experiments. The unsuccessful high angle of attack emulation of the wet behavior by trip strips at the 5% chord location may have been caused by the trip strips placed aft of the leading edge separation point as shown in figure 4.7. In this position, the trip strips would be ineffective.

Similar transition effects on separation behavior has been demonstrated on a sphere where separated regions were

decreased by forcing boundary layer transition prematurely[1].
In addition, performance increases and flow reattachment have
been observed at high angles of attack for airfoils subjected
to extreme sound levels[7]. The mechanism is thought to be
similar to the premature boundary layer transition caused by
rain, but is not well understood.

4.5.2 The NACA 0012 Airfoil

The NACA 0012 airfoil exhibits similar high angle of
attack behavior to the NACA 64-210 airfoil. The NACA 0012
airfoil in dry conditions has a rather drastic stall at 14°
angle of attack (figure 4.2). In rain conditions however,
stall is delayed to 18°.

Figure 4.17 shows the rapid lift increase for the NACA
0012 airfoil at 15° angle of attack when rain is initiated.
In dry conditions, the NACA 0012 airfoil is fully stalled
with separation present near the leading edge. When rain is
initiated, the increased turbulence is thought to help the
boundary layer remain attached farther along the airfoil.
This explains the rapid increase of lift in the time-
dependent output. Even though the increased performance at
high angles of attack is believed to be caused by premature
transition, it was not emulated by the trip strip
experiments. As with the NACA 64-210 airfoil, the trip
strips may have been located aft of the dry leading edge
separation point.
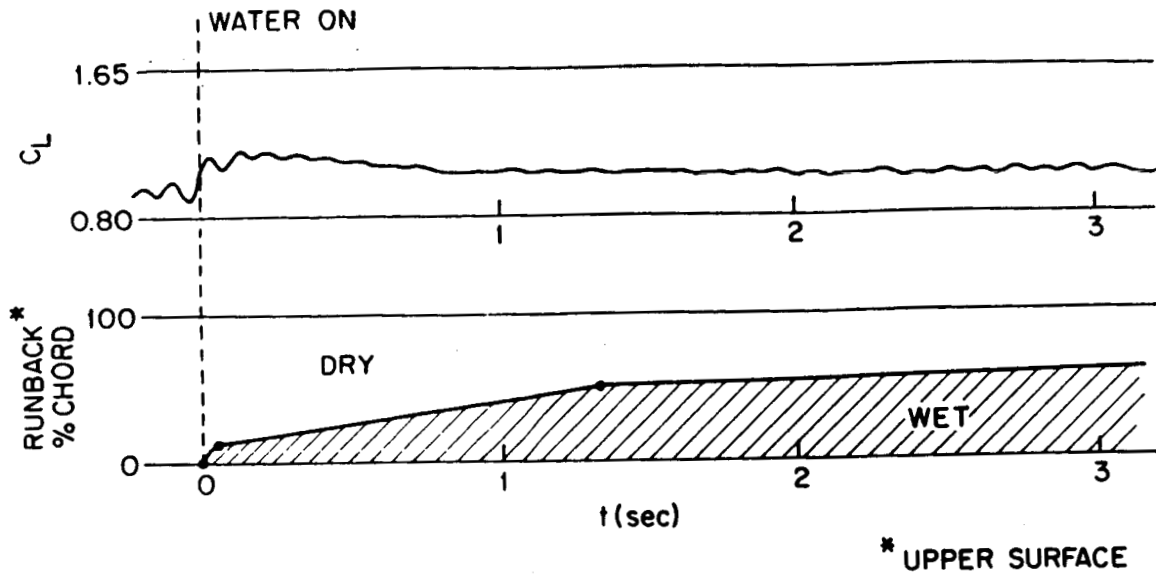
Figure 4.17. Time-dependent lift and water runback position for the NACA 0012 airfoil at 15° angle of attack.

The water runback behavior is also shown in figure 4.17. Downstream of 60% chord, the water runback became nearly stagnant which indicates that a trailing edge separation is present in that vicinity. The trailing edge separation in wet conditions does not degrade the airfoil performance as much as the leading edge separation which occurs in dry conditions.

In addition to the immediate lift degradation observed in figure 4.17, a longer time scale lift degradation is seen which corresponds to the time scale of the water runback behavior. This is thought to be caused by similar mechanisms to those observed at lower angles of attack where the water layer appears to alter the airfoil geometry.

4.5.3 The Wortmann FX67-K170 Airfoil

At high angles of attack in dry conditions, the stall behavior of the Wortmann airfoil is complicated (figure 4.1) due to low Reynolds number effects where various separation mechanisms, such as those described in section 2.2.1, may be present. In contrast, the high angle of attack behavior in wet conditions (figure 4.1) is typical of a turbulent boundary layer stall process. The stall is gradual as the trailing edge boundary layer separation point moves forward with increasing angle of attack. The high angle of attack behavior for the Wortmann airfoil was emulated by forcing premature transition (figure 4.4). This supports the idea that the differences in the dry and wet stall processes are caused by boundary layer effects.
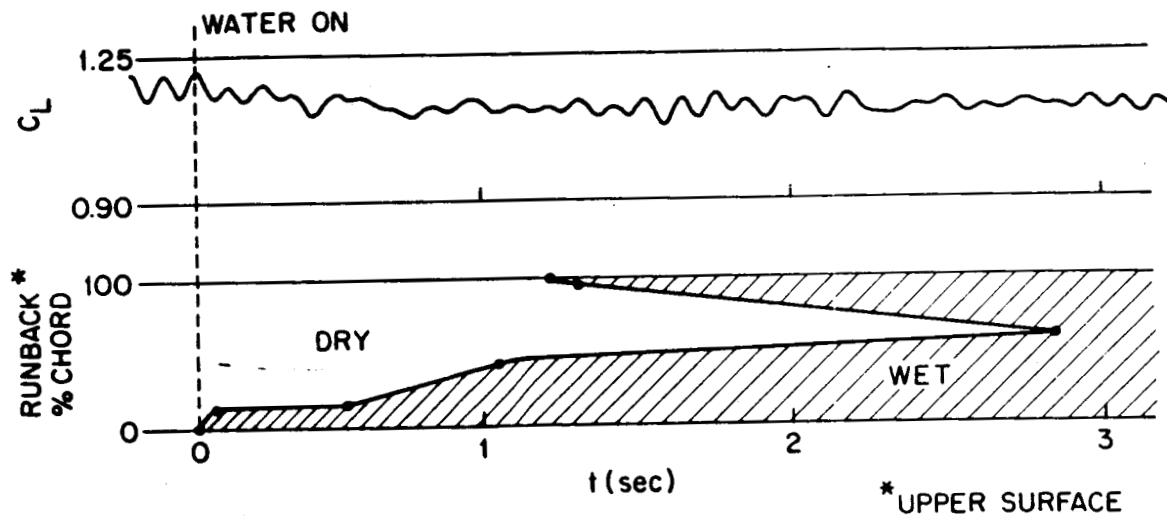

Figure 4.18. Time-dependent lift and water runback position for the Wortmann FX67-K170 airfoil at 15° angle of attack.

Figure 4.18 shows the lift output and water runback behavior as a function of time for the Wortmann airfoil at 15° angle of attack when rain is initiated. The decrease in lift is expected to occur immediately after rain initiation, since it is believed to be caused by a leading edge premature transition mechanism. However, the lift degradation occurs slowly at time scales consistent with water runback behavior. The reason for this discrepancy is not clearly understood.

4.6 Surface Chemistry Effects

Each of the three airfoils were waxed to study the effects of increasing the contact angle in wet conditions. The contact angle was altered from approximately 50° to nearly 90° by waxing the airfoil. Both steady-state and time-dependent force data was measured.

The overall lift curves are shown in figures 4.19, 4.20, and 4.21 for the three airfoils when waxed. For all three airfoils at angles of attack prior to stall initiation, the performance degradation was exaggerated in wet conditions as a result of waxing the airfoils. At angles of attack above stall initiation however, similar performance was observed for the waxed and unwaxed airfoils in wet conditions.

Time-dependent lift output and runback behavior graphs for the waxed cases are presented in figures 4.22, 4.23, and 4.24 for the Wortmann airfoil at 2°, the NACA 0012 at 2°, and the NACA 64-210 at 1° angle of attack. These results are
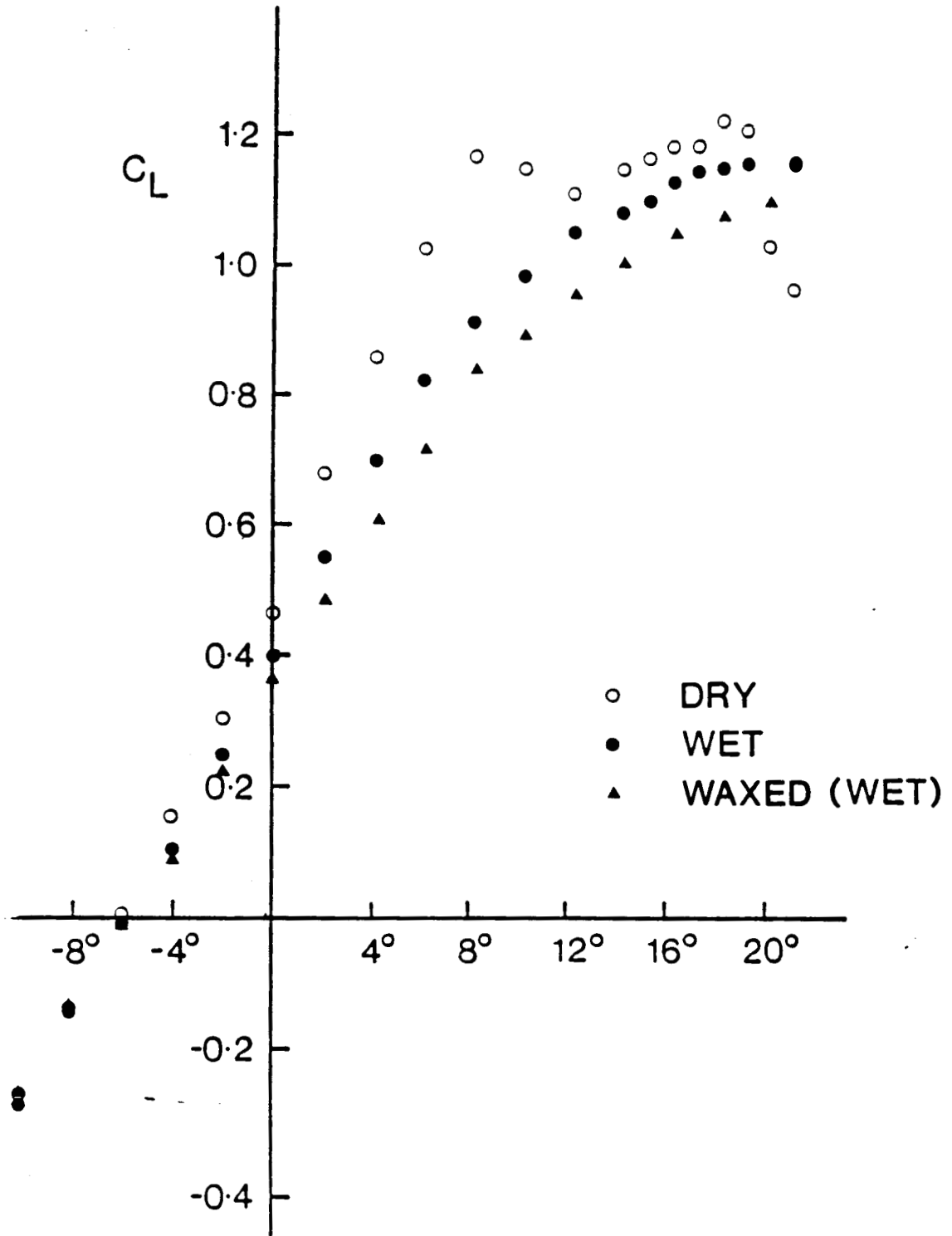
Figure 4.19. Comparison of the dry, wet, and waxed lift polars for the Wortmann FX67-K170 airfoil.
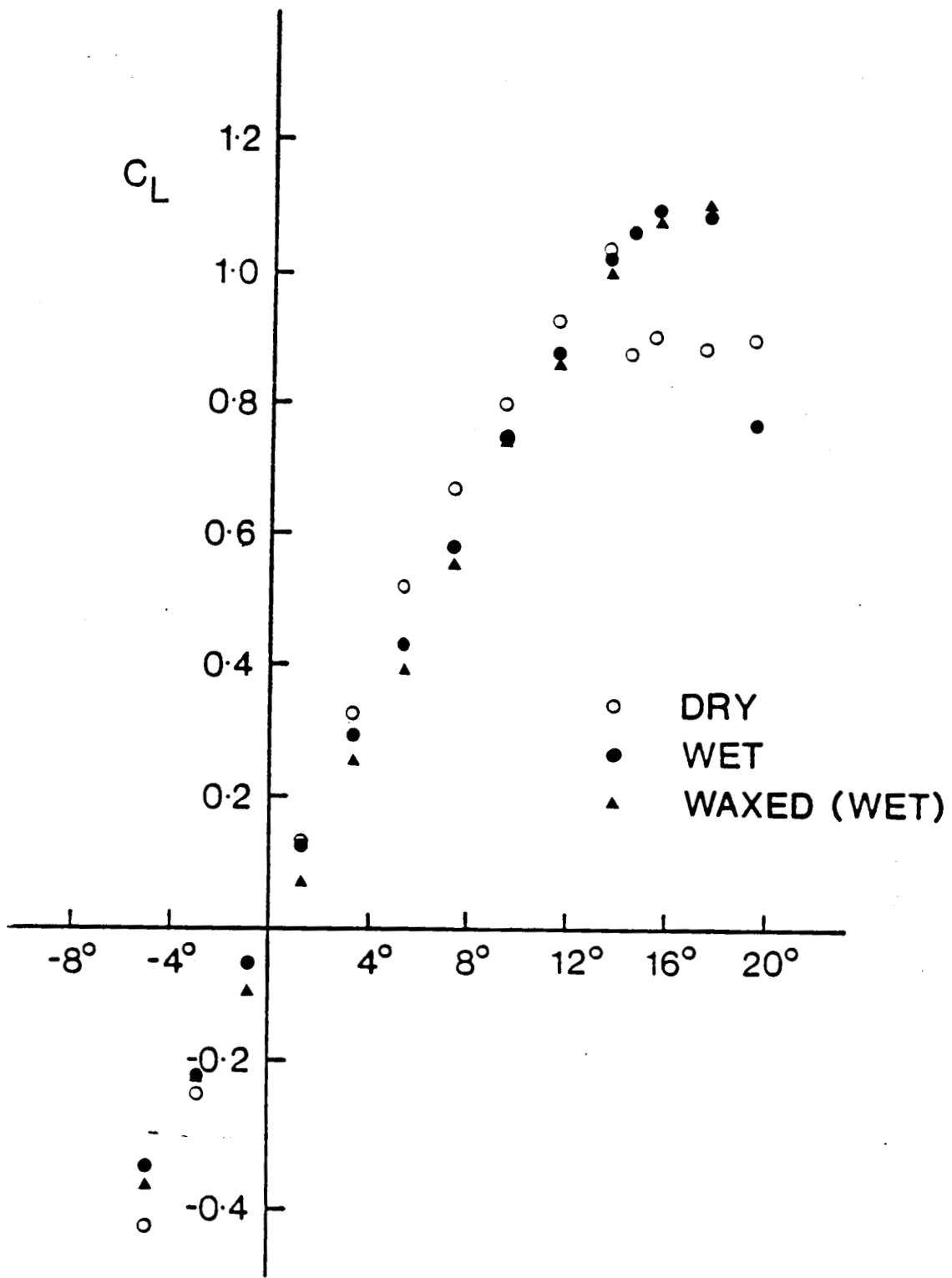
Figure 4.20.   Comparison of the dry, wet, and waxed lift
polars for the NACA 0012 airfoil.
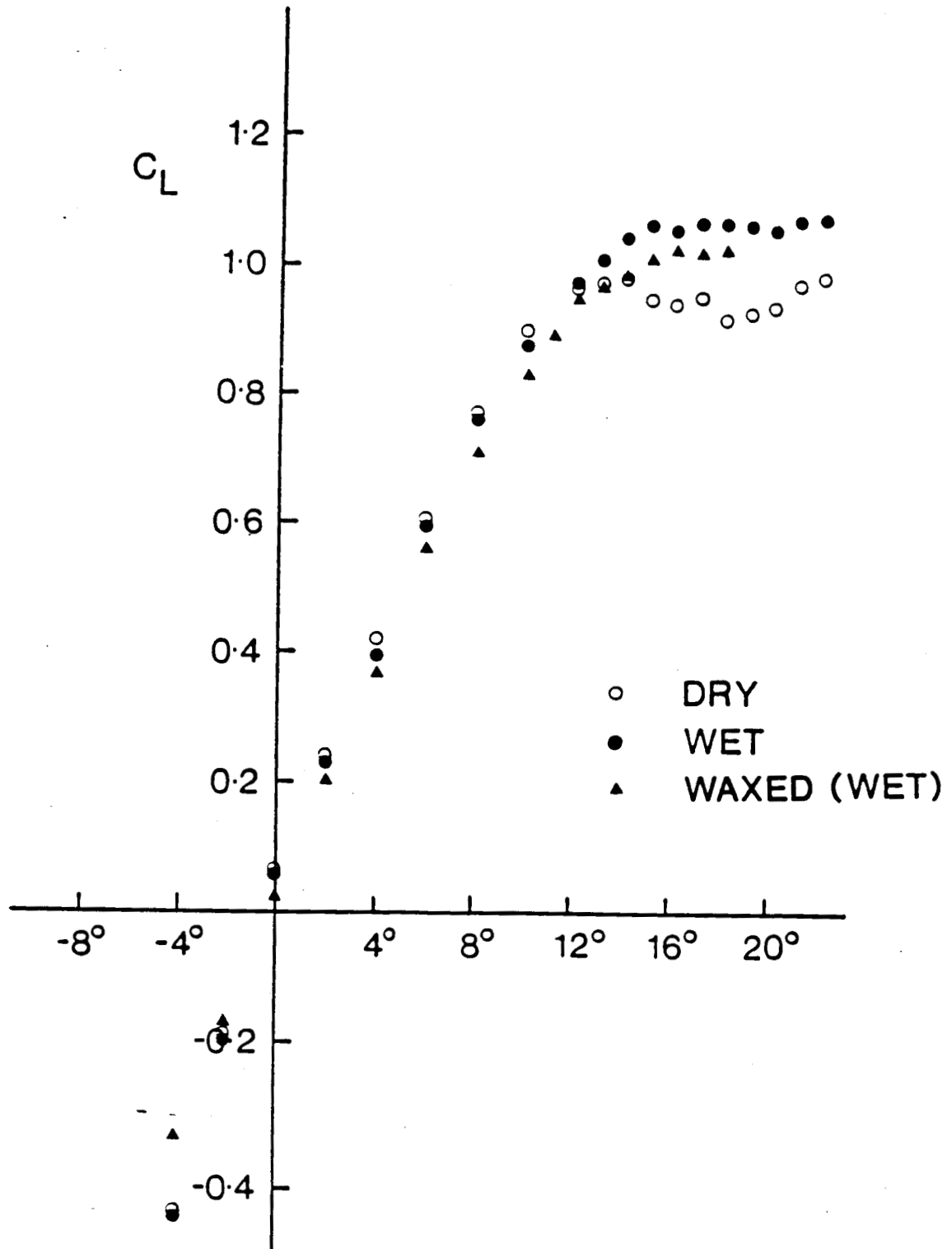
Figure 4.21. Comparison of the dry, wet, and waxed lift
polars for the NACA 64-210 airfoil.

similar to the time-dependent data presented for the unwaxed airfoils (figures 4.8, 4.13, 4.14). Both short and long time scale effects are observed.

Water runback behavior differed slightly in the waxed case compared to the unwaxed case. Normally, for all three airfoils, rivulets were not formed in the runback process. The water droplets tended to runback individually which is a direct result of the increased contact angle. In addition, the overall runback pattern generally took longer to developed compared to the unwaxed case.
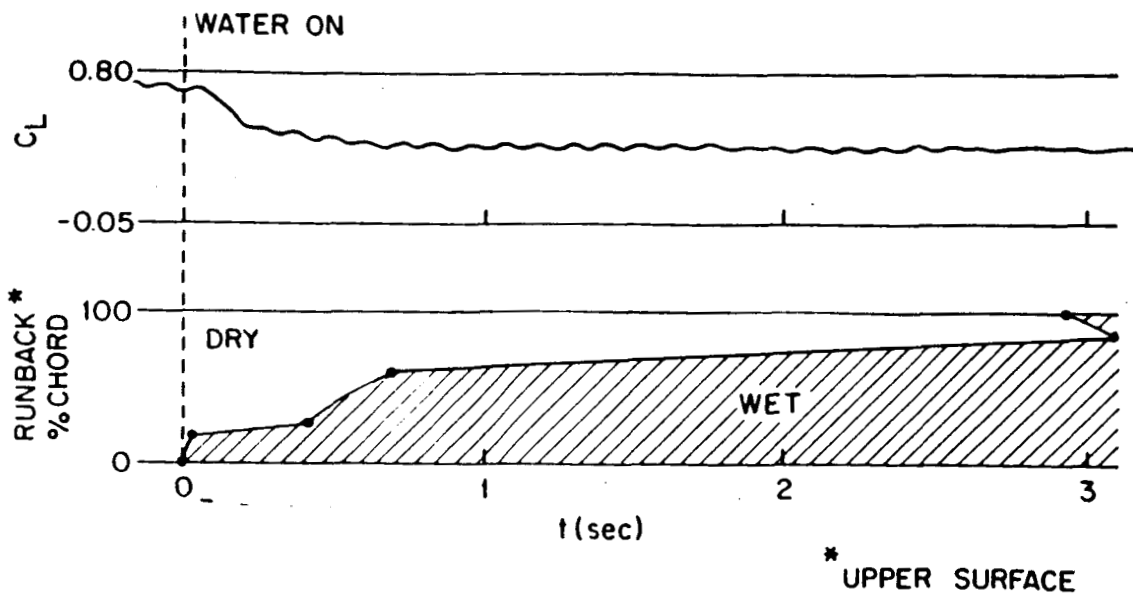
Figure 4.22. Time-dependent lift and water runback position for the Wortmann FX67-K170 airfoil at 2° angle of attack when waxed.

94
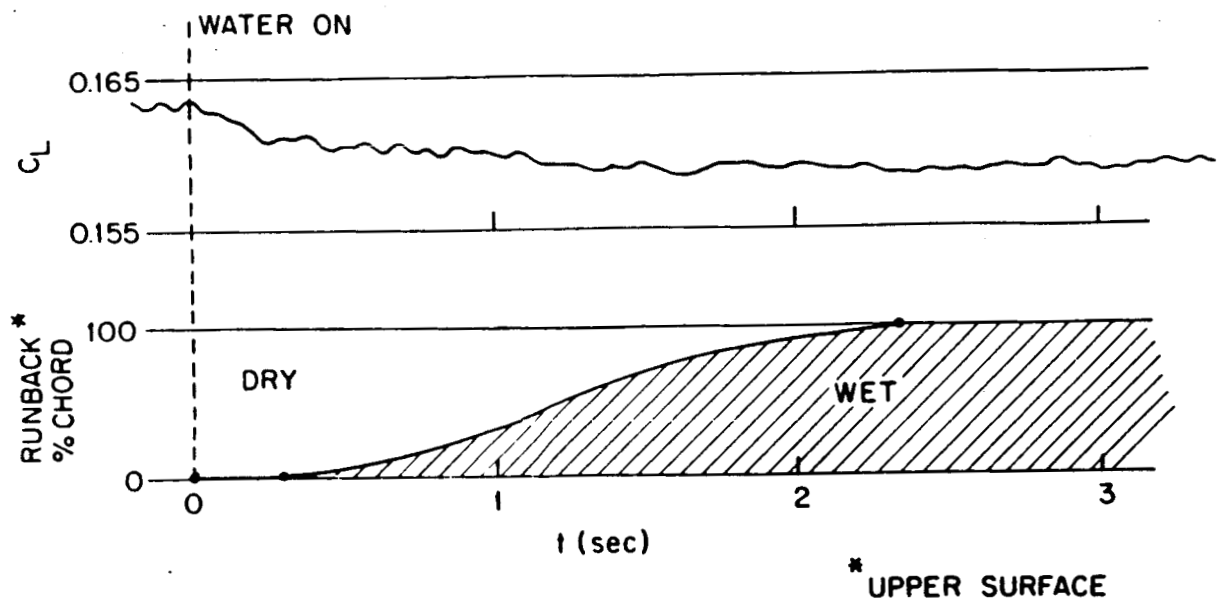
Figure 4.23. Time-dependent lift and water runback position
for the NACA 0012 airfoil at 2° angle of attack when waxed.
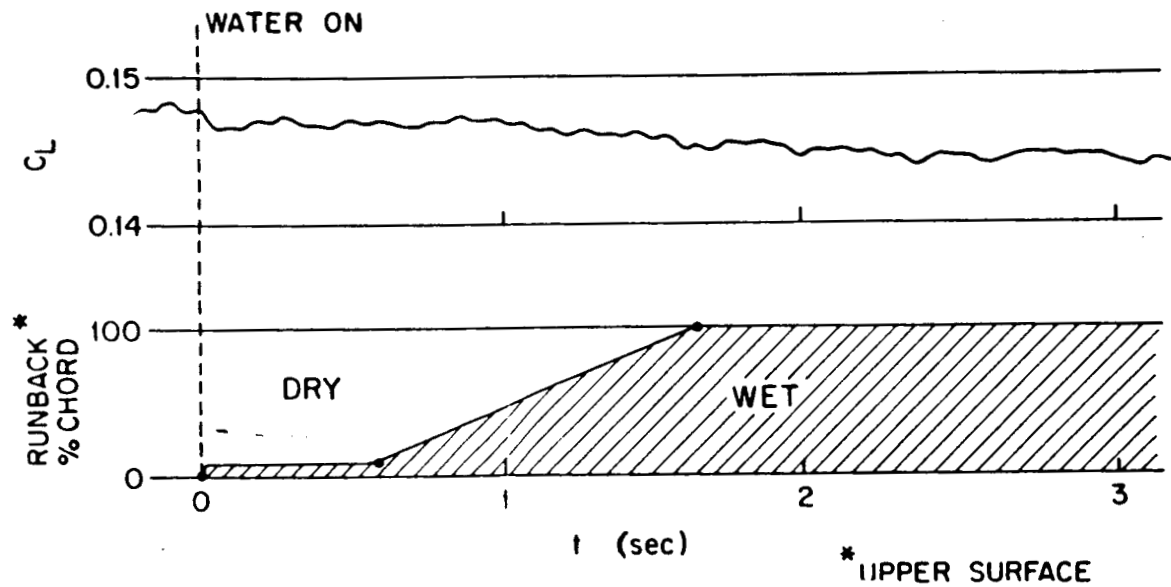
Figure 4.24. Time-dependent lift and water runback position
for the NACA 64-210 airfoil at 1° angle of attack when
waxed.

Figures 4.25, 4.26, and 4.27 show a direct comparison of the waxed and unwaxed time-dependent lift output by combining the time-dependent data from this section with the data from section 4.4. The additional steady-state lift degradation measured for the waxed airfoils can be seen. The surface chemistry effects do not appear to alter the magnitude of the fast, leading edge roughness mechanism which induces premature boundary layer transition. However, the increased contact angle does seem to have an effect on the longer time scale mechanisms. The waxed surface may induce a thicker water layer which would alter the airfoil geometry further than for the unwaxed airfoils. Again, this longer time scale mechanism is likely enhanced in these small scale tests as discussed in section 2.3.5.
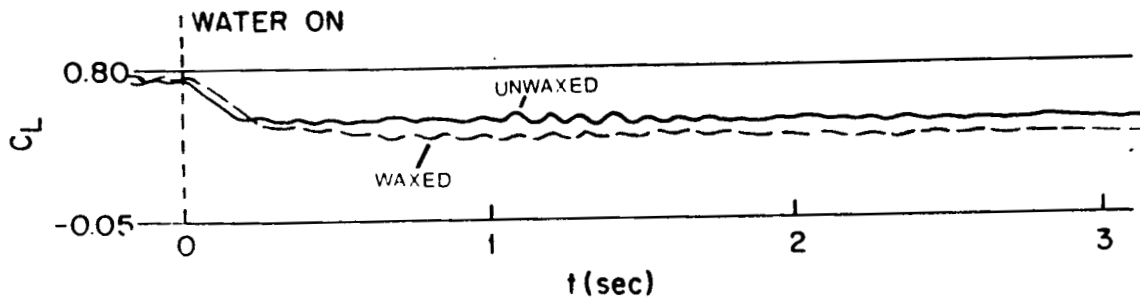
Figure 4.25. Comparison of the waxed and unwaxed time-dependent lift behavior for the Wortmann FX67-K170 airfoil at 2° angle of attack.
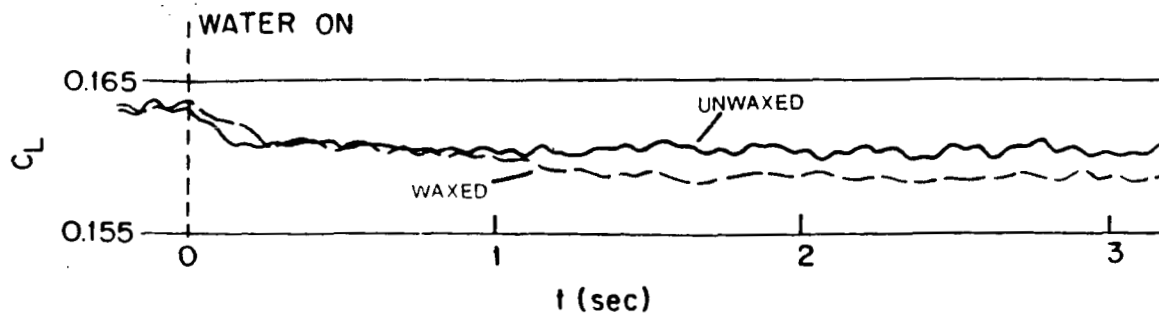
Figure 4.26.   Comparison of the waxed and unwaxed time-
dependent lift behavior for the NACA 0012 airfoil at 2°
angle of attack.
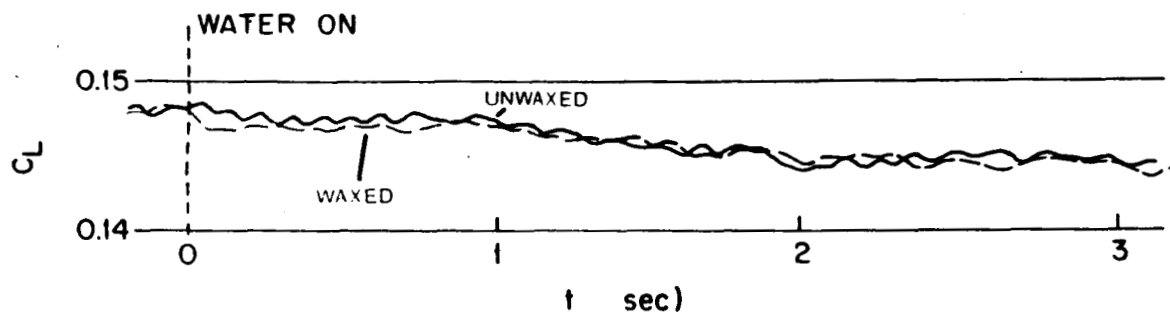
Figure 4.27.   Comparison of the waxed and unwaxed time-
dependent lift behavior for the NACA 64-210 airfoil at 1°
angle of attack.

Chapter 5

SUMMARY

Wind tunnel experiments at a Reynolds number of 310,000 and rain rate of 1000 mm/hr were conducted in dry and wet conditions to compare the quantitative and qualitative aerodynamic performance degradation of a Wortmann FX67-K170, a NACA 0012, and a NACA 64-210 airfoil in heavy rain conditions. Various experiments were conducted to determine the mechanisms which alter the airfoils' aerodynamic performance in heavy rain conditions. Both steady-state, dry and wet conditions, as well as time-dependent, transient effects were investigated. Lift and drag measurements were recorded for various test conditions.

Because of the complex physical phenomena involving both time and spacial variables, unique techniques were developed to visualize aerodynamic and water behavior. A video camera was strobe synchronized to generate detailed photographs of the water runback behavior. A method was developed to protect the microtufts and allow their use in wet conditions. Liquid crystals were used to visualize boundary layer behavior, and a video camera aided in analysis. In addition to the experimental flow visualization techniques, a compressible, viscid airfoil computational fluid dynamics code was employed to gain additional insight into the airfoils' boundary layer aerodynamics.

Test results indicate that the mechanism which most significantly effects aerodynamic performance for the airfoils in wet conditions at low Reynolds numbers is premature boundary layer transition generated at the leading edge immediately upon entering the rain condition. This effect caused performance degradation for all three airfoils at angles of attack below stall initiation. Lift was decreased by as much as 25% for the Wortmann airfoil, and drag increased by approximately 20% for all three airfoils.

At high angles of attack, the premature boundary layer transition had the effect of reducing the separated flow regions and suppressing stall for the NACA 64-210 and NACA 0012 airfoils. For the Wortmann airfoil at high angles of attack, lift was still reduced in wet conditions, but the lift curve was smoothed as a result of the transition behavior.

The magnitude to which the airfoils were affected by rain varied greatly between the airfoils and appeared to be related to the susceptibility of each airfoil to premature boundary layer transition. The Wortmann airfoil, which is a naturally laminar flow airfoil, showed significant performance degradation in heavy rain conditions due to premature boundary layer transition. The NACA 0012 airfoil showed some losses in heavy rain, and the NACA 64-210 airfoil showed minimal degradation. However, in these low Reynolds number tests, all the airfoils (at low angles of attack)

C-2

generally had extensive laminar boundary layer regions. Therefore, the susceptibility of the airfoils to rain appears to be directly related to the importance of laminar flow for the aerodynamic performance of each airfoil.

The varied performance degradation of the airfoils in heavy rain conditions could be emulated at low angles of attack by forcing boundary layer transition at 5% chord on the top surface of the NACA 64-210 and NACA 0012 airfoils and by forcing transition at 25% chord on the top surface of the Wortmann airfoil. At higher angles of attack, the wet performance could not be emulated by the roughness elements for the NACA 0012 or 64-210 airfoils. This is thought to be due to the location of the roughness elements aft of the dry boundary layer separation point.

A secondary mechanism which altered the airfoils' performance was observed in these tests over longer time scales consistent with the water runback behavior. The water layer is believed to effectively alter the airfoil geometry. Performance losses due to these secondary effects was nearly equivalent for all three airfoils. It should be noted, however, that because of the small scale of the models employed in these experiments, the ratio of the water layer thickness to the chord length is artificially high. Therefore, the significance of the secondary effects is likely enhanced in these small scale tests, and care should be exercised when extrapolating these effects to full scale

applications.

When the airfoil surface chemistry was altered by waxing the airfoils, the aerodynamic performance degradation at low angles of attack in wet conditions was further exaggerated as compared to the unwaxed cases. However, waxing the airfoils had very little effect on the wet performance behavior of the airfoils at high angles of attack. The wax surface is believed to increase the thickness of the water layer present on the airfoil surface which results in additional performance degradation at low angles of attack.

In conclusion, the most important mechanism which results in aerodynamic performance degradation in rain conditions appears to be a premature boundary layer transition induced immediately upon entering the rain condition. Secondary water runback effects were observed in these tests, but are likely exaggerated due to the small testing scale. The susceptibility of an airfoil at low Reynolds numbers in heavy rain conditions appears to be highly dependent on the importance of the laminar boundary layer behavior for the airfoil's performance. This effect can be determined for specific airfoils by forced transition experiments in dry conditions.

REFERENCES

1. Batchelor, G.K., <u>An Introduction to Fluid Dynamics</u>, Cambridge University Press, 1967, Figure 5.11.7 and Figure 6.12.7.

2. Presentation by Bezos, G., "NASA Tests," Second Annual Workshop on the Effects of Rain on Aerodynamics, NASA Langley Research Center, May 7-8, 1986.

3. Bilanin, A.J., "Scaling Laws for Testing of High Lift Airfoils Under Heavy Rainfall," AIAA-85-0237, January, 1985.

4. Bisplinghoff, R.L. and Ashley, H., <u>Principles of Aeroelasticity</u>, Dover Publications Inc., 1962, pp 114-125.

5. Brun, R.J., Gallagher, H.M., and Vogt, D.E., "Impingement of Water Droplets on NACA 65-208 and 65-212 Airfoils at 4° Angle of Attack," NACA TN 2952, 1953.

6. Chang, H.P. and Kimble, K.R., "Influence of Multidrop Size Distribution on Icing Collection Efficiency," AIAA-83-0110, January, 1983.

7. Collins, F.G. and Zelenevitz, J., "Influence of Sound upon Separated Flow over Wings," <u>AIAA Journal</u>, Volume 13, March, 1975.

8. Drela, M., "Two-Dimensional Transonic Aerodynamic Design and Analysis Using the Euler Equations," PhD thesis, Department of Aeronautics and Astronautics, Massachusetts Institute of Technology, 1985.

9. Personal Communication with Professor Mark Drela, Massachusetts Institute of Technology, September, 1986.

10. Dunham, R.E., "Potential Influences of Heavy Rain on General Aviation Airplane Performance," AIAA-86-2606, September, 1986.

11. Dunham R.E., Bezos, G.M., Gentry, C.L., and Melson, E., "Two-Dimensional Wind Tunnel Tests of a Transport-Type Airfoil in a Water Spray," AIAA-85-0258, January, 1985.

12. Giles, M.B., "Newton Solution of Steady Two-Dimensional Transonic Flow," PhD thesis, Department of Aeronautics and Astronautics, Massachusetts Institute of Technology, 1985.

13. Gelder, T.F., Smyers, W.H., von Glahn, U., "Experimental Droplet Impingement on Several Two-Dimensional Airfoils with Thickness Ratios of 6 to 16 Percent," NACA TN 3839, December, 1956.

14. Greiner, C.M., "The Statics and Dynamics of Sessile Bubbles on Inclined Surfaces," MS thesis, Department of Aeronautics and Astronautics, Massachusetts Insititute of Technology, 1985.

15. Haines, P. and Luers, J., "Aerodynamic Penalties of Heavy Rain on Landing Airplanes," Journal of Aircraft, Vol. 20, No. 2, February, 1983, pp 111-119.

16. Hansman, R.J. and Barsotti, M.F., "The Aerodynamic Effect of Surface Wetting Characteristics on a Laminar Flow Airfoil in Simulated Heavy Rain," AIAA-85-0260, January, 1985.

17. Hershfield, D.M., "Estimating the Extreme-Value 1 Minute Rainfall," Journal of Applied Meteorology, Vol. 11, No. 6, 1972, pp 936-940.

18. Holmes, B.J., Croom, C.C., Gall, P.D., Manuel, G.S., and Carraway, D.L., "Advanced Boundary Layer Transition Measurement Methods for Flight Applications," AIAA-86-9786, 1986.

19. Mueller, T.J., "Low Reynolds Number Vehicles," AGARD No. AG-288, 1985.

20. Presentation by Mulally, A.R., "Lessons Learned From Wind Shear Encounters," 1984 SAE Aerospace Congress & Exposition, Long Beach, California, October 15-18, 1984.

21. Pruppacher, H.R. and Klett, J.D., Microphysics of Clouds and Precipitation, D. Reidel Publishing Co., 1978, p. 23.

22. Rae, W. and Pope, A., Low Speed Wind Tunnel Testing, John Wiley and Sons, 1984, pp. 449-456.

23. Rhode, R.V., "Some Effects of Rainfall on Flight of Airplanes and on Instrument Indications," NACA TN 803, April, 1941.

24. Riordan, P., "Weather Extremes Around the World," Earth Sciences Laboratory, TR-70-45-es, 1970.

APPENDIX: Airfoil Coordinates

1) Wortmann Airfoil Coordinates:

NR	X/T	YO/T	YU/T
1	1.00000	0.00000	0.00000
2	0.99893	0.00027	0.00005
3	0.99572	0.00113	0.00022
4	0.99039	0.00243	0.00044
5	0.98296	0.00415	0.00076
6	0.97347	0.00631	0.00105
7	0.96194	0.00891	0.00124
8	0.94844	0.01201	0.00124
9	0.93301	0.01566	0.00072
10	0.91573	0.01991	0.00037
11	0.89668	0.02548	-0.00148
12	0.87592	0.03040	-0.00197
13	0.85355	0.03689	-0.00386
14	0.82967	0.04437	-0.00325
15	0.80438	0.05287	-0.00913
16	0.77779	0.06229	-0.01236
17	0.75000	0.07233	-0.01572
18	0.72114	0.08259	-0.01896
19	0.69134	0.09263	-0.02187
20	0.66072	0.10208	-0.02437
21	0.62941	0.11063	-0.02654
22	0.59755	0.11808	-0.02844
23	0.56526	0.12429	-0.03012
24	0.53270	0.12919	-0.03155
25	0.50000	0.13274	-0.03272
26	0.46730	0.13490	-0.03365
27	0.43474	0.13571	-0.03435
28	0.40245	0.13526	-0.03480
29	0.37059	0.13370	-0.03501
30	0.33928	0.13119	-0.03499
31	0.30866	0.12783	-0.03474
32	0.27886	0.12365	-0.03425
33	0.25000	0.11870	-0.03354
34	0.22221	0.11305	-0.03261
35	0.19562	0.10677	-0.03146
36	0.17033	0.09994	-0.03011
37	0.14645	0.09263	-0.02856
38	0.12408	0.08490	-0.02682
39	0.10332	0.07685	-0.02490
40	0.08427	0.06856	-0.02282
41	0.06699	0.06011	-0.02062
42	0.05156	0.05158	-0.01827
43	0.03806	0.04309	-0.01580
44	0.02653	0.03487	-0.01321
45	0.01704	0.02765	-0.01057
46	0.00961	0.02012	-0.00815
47	0.00428	0.01292	-0.00514
48	0.00107	0.00653	-0.00217
49	0.00000	0.00000	0.00000

2) NACA 0012 Airfoil Coordinates:

x (per cent c)	y (per cent c)	$(v/V)^2$	v/V	$\Delta v_a/V$
0	0	0	0	1.988
0.5	.....	0.640	0.800	1.475
1.25	1.894	1.010	1.005	1.199
2.5	2.615	1.241	1.114	0.934
5.0	3.555	1.378	1.174	0.685
7.5	4.200	1.402	1.184	0.558
10	4.683	1.411	1.188	0.479
15	5.345	1.411	1.188	0.381
20	5.737	1.399	1.183	0.319
25	5.941	1.378	1.174	0.273
30	6.002	1.350	1.162	0.239
40	5.803	1.288	1.135	0.187
50	5.294	1.228	1.108	0.149
60	4.563	1.166	1.080	0.118
70	3.664	1.109	1.053	0.092
80	2.623	1.044	1.022	0.068
90	1.448	0.956	0.978	0.044
95	0.807	0.906	0.952	0.029
100	0.126	0	0	0
L.E. radius: 1.58 per cent c				

NACA 0012 Basic Thickness Form

3) NACA 64-210 Airfoil Coordinates:

NACA 64-210

(Stations and ordinates given in
per cent of airfoil chord)

Upper surface		Lower surface	
Station	Ordinate	Station	Ordinate
0	0	0	0
0.431	0.867	0.569	− 0.767
0.673	1.056	0.827	− 0.916
1.163	1.354	1.337	− 1.140
2.401	1.884	2.599	− 1.512
4.890	2.656	5.110	− 2.024
7.387	3.248	7.613	− 2.400
9.887	3.736	10.113	− 2.702
14.894	4.514	15.106	− 3.168
19.905	5.097	20.095	− 3.505
24.919	5.533	25.081	− 3.743
29.934	5.836	30.066	− 3.892
34.951	6.010	35.049	− 3.950
39.968	6.059	40.032	− 3.917
44.985	5.938	45.015	− 3.748
50.000	5.689	50.000	− 3.483
55.014	5.333	54.987	− 3.143
60.025	4.891	59.975	− 2.749
65.033	4.375	64.967	− 2.315
70.038	3.799	69.962	− 1.855
75.040	3.176	74.960	− 1.386
80.038	2.518	79.962	− 0.926
85.033	1.849	84.968	− 0.503
90.024	1.188	89.977	− 0.154
95.012	0.564	94.988	0.068
100.000	0	100.000	0

L.E. radius: 0.720
Slope of radius through L.E.: 0.084